Multiscale investigation on the formation path of the apatite phase in bioactive glasses

Amira Ghneim, Lea Abou Samra, Dominik Schaniel, Samantha Soule, Cédric Carteret, El-Eulmi Bendeif

Multiscale Investigation on the Formation Path of the Apatite Phase in Bioactive Glasses

GHNEIM Amira[a,1], ABOU SAMRA Lea[a,2], SCHANIEL Dominik[a,3], SOULE Samantha[b,1], CARTERET Cédric[b,2] & BENDEIF El-Eulmi [a,4]*

[a]University of Lorraine, CNRS, CRM2, UMR 7036, 54506 Vandoeuvre-lès-Nancy cedex, France

[a,1]*amira.ghneim@univ-lorraine.fr,* [a,2]*lea.abou-samra5@etu.univ-lorraine.fr,* [a, 3]*dominik.schaniel@univ-lorraine.fr,* [a,4]*el-eulmi.bendeif@univ-lorraine.fr*

[b]University of Lorraine, CNRS, LCPME, UMR 7564, 54600 Villers-lès-Nancy, France

[b,1]*samantha.soule@univ-lorraine.fr,* [b,2]*cedric.carteret@univ-lorraine.fr*

*Corresponding author : Laboratoire CRM² (UMR-CNRS 7036), Faculté des Sciences et Technologies, BP 70239, Campus, Bd des Aiguillettes, 54506 Vandoeuvre les Nancy, Cedex, France.
Tel:+33(0)372745634, Fax: +33(0)372745218
E-mail: el-eulmi.bendeif@univ-lorraine.fr

Abstract: Mesoporous bioactive glasses (MBGs) have been reported as promising biomaterials to be able to stimulate and promote the bones' growth. When exposed to simulated body fluid (SBF), MBGs develop an apatite phase called carbonate-hydroxyapatite (HCA) on their surfaces that closely mimic the mineral phase of the bones. In order to gain deeper insights on the key stages of surface reactions of two different types of MBGs (58S and 70S30C) soaked in SBF, we have used high energy total X-ray scattering coupled to pair distribution function analysis, along with Raman spectroscopy and scanning electron microscopy. This type of coupled analytical approach can ultimately help to unravel the details of the reaction kinetics in the complex calcium phosphate environment around the BGs surfaces. The data obtained in our in-vitro study point to the formation of other intermediate phases like amorphous calcium phosphate and calcite, that transform after a specific time into a HCA depending on the composition of the MBGs, their surface properties and their interaction times with SBF.

Keywords: Bioactive Glasse, Total X-ray scattering, Raman spectroscopy, Carbonate-Hydroxyapatite, Amorphous Calcium Phosphate.

1. Introduction

Since their discovery in 1969 by Hench [1], the bioactive glasses (BGs) have gone a long way in investigations. Nowadays, they are used in some applications relying on bone regeneration and tissue engineering such as filling cavities and dental, maxillofacial, and orthopedic surgery [2-6]. However, they still suffer from some drawbacks such as comparatively lower mechanical stability or other unwanted effects such as crystallization during sintering [7], that could be overcome by a detailed understanding of how the glass composition affects the crystallization [8] or by exploiting the tremendous possibilities offered by the sol-gel synthesis of BGs [9,10]. While the sol-gel process offers a high flexibility for functionalizing the porous BGs for various purposes, including drug delivery [11], the complexity of these materials requires multi-technique approaches to investigate the key steps in the bone-building

process. In the last decades a plethora of methods has been used to assess the bioactivity, i.e. the ability of the bioglass to bond to bone tissue and have helped to understand the key steps of the BG reaction mechanism after being exposed to simulated body fluid (SBF) in *in-vitro* experiments [12]. This mechanism, first proposed by Hench [13], can be summarized as follows (**Fig. 1.**) [14-16]:

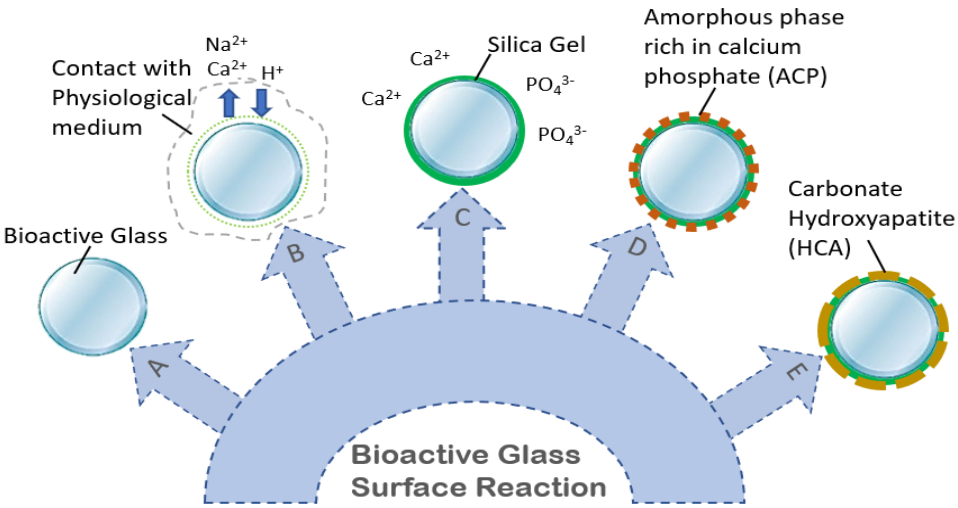

Fig. 1. presents the first five steps of the bioactivity process of the bioactive glass as outlined by Hench.

The first two steps (Stage A & B) consist in a rapid cation exchange of Na^+ and/or Ca^{2+} with H^+ from solution, creating silanol bonds (Si–OH) on the glass surface. The pH of the solution increases and a silica-rich (cation-depleted) region forms near to the glass surface. Phosphates can also be lost from the glass if they are present in the composition. Furthermore, the high local pH contributes in breaking Si–O–Si bonds, by attacking the silica glass network by OH. Soluble silica is lost in the form of $Si(OH)_4$ toward the solution, leaving more Si–OH (silanols) at the glass–solution interface. In the third step (Stage C), the Si–OH groups near the glass surface condense, resulting in a repolymerization of the silica-rich layer. The fourth step (Stage D) involves the migration of Ca^{2+} and PO_4^{3-} groups from the BG itself and the bodily fluid, leading to the formation of an amorphous film rich in $CaO–P_2O_5$ on the silica-rich layer. Finally, by referring to Stage E, the incorporation of hydroxyls and carbonate ions from solution contribute to the crystallization of the $CaO–P_2O_5$ film, resulting in carbonate hydroxyapatite (H(C)A) formation ($Ca_{10}(PO_4)_{6-x}(CO_3)_x(OH)_2$).

As outlined, e.g., in Cerruti's review [17], these different steps have been investigated by several analytical techniques in order to further explore and study the compositions and developments of silica gel and the different phosphate phases. For instance, Solid-State multinuclear magnetic resonance (NMR) [18-26], various spectroscopies like Raman and Fourier transform infrared [15, 27-36], X-ray photo-electron [36], particle-induced X-ray emission [37,38], X-ray diffraction (XRD) [15,18-20,33,34,39,40] as well as scanning electron microscopy coupled with Electron dispersive X-ray Spectroscopy

[20,27-33,35,41-46] have been used for these investigations in order to support and validate the theory of Hench.

However, there are still some unresolved issues and in particular the different length and time scales involved in the formation of the H(C)A phase pose a constant challenge on the overall characterization of the bioactivity of BGs. To overcome this challenge, an advanced in-situ total X-ray scattering technique coupled to PDFs analysis has been developed by FitzGerald and his colleagues [47] to understand the atomic structure of the complex amorphous bioactive materials and study their interactions with a physiological medium. This type of method could push the boundaries of a detailed structural characterization and understanding of the reaction mechanism even further in complement to the hitherto predominantly used analytical methods. Thus, in order to obtain quantitative information on the different species that appear during the H(C)A formation, we propose to use a differential PDF approach along with a singular value decomposition (SVD) analysis. Moreover, Raman spectroscopy and scanning electron microscopy coupled to EDS are employed as complementary techniques to corroborate the findings of the total scattering study. We focused on two different prototypic bioactive glasses: 58S and 70S30C in order to gain a comprehensive understanding on the different stages of the formation of carbonate hydroxyapatite and shed light on their structural changes that occur on the atomic level. Both BGs have predominantly amorphous structure, which makes it easier to track the formation and development of any phases on their surfaces once they are immersed in SBF. By performing a quantitative analysis of the evolution of the different phases after immersion in SBF based on a combination of differential PDF analysis and Raman spectroscopy, our work might serve as an important methodological reference for future studies, allowing for structural characterization of the BGs on several length scales and in particular enables us to follow the evolution of amorphous phases, that are critical in the H(C)A formation.

2. Materials and Methods:

2.1 Sol-Gel Synthesis

Two types of bioactive glasses, namely 70S30C (70% SiO_2, 30% CaO (mol. %)) and 58S (60% SiO_2, 36% CaO, 4% P_2O_5 (mol. %)), were synthesized through the standard sol-gel method. The main precursors used were tetraethyl orthosilicate (TEOS) (≥98.0%, Acros Organics), and calcium nitrate tetrahydrate ($Ca(NO_3)_2.4H_2O$) (CaN) (≥97.0%, Thermo Scientific). Triethyl phosphate (TEP) (≥99.8%, Sigma-Aldrich) was also used in the case of the ternary glass 58S. Initially, distilled water was stirred magnetically at either 60°C or room temperature to prepare binary and ternary bioglasses, respectively. Then, 9.33 g of TEOS and/or 0.7144g of TEP were added dropwise to the mixture and stirred until a clear solution was obtained. The molar ratio between the distilled water and TEOS precursor was fixed at 8 and a few drops of an acidic solution were added to ensure complete hydrolysis of the silicate precursor. The $Ca(NO_3)_2.4H_2O$ powder was slowly added to the solution and stirred until a gel was formed. Subsequently, for 58S, the gel was aged at 60°C for 55 h, dried at 180°C for 72 h, and then calcinated at 700°C for 3 h. While for 70S30C, the aging, the drying,

and calcination processes were followed according to the protocol reported in the article [48].

2.2 Characterization of BGs

The nitrogen adsorption desorption measurements were conducted by using a *Microtrac-BELSROP-Max* instrument at 77K in order to determine the structural textures of all the desired materials (refer to **Table 1**). The specific surface area for BGs were determined by the *Brunauer-Emmett-Teller* (BET) method while the *Barret-Joyner-Halanda* (BJH) method was used to determine the sizes and volumes of the BGs pores from the desorption curves. Prior to the analysis the samples were kept under vacuum for an hour to re-degas. The surface morphology of the bioglasses was also investigated using scanning electron microscopy (SEM) (*JEOL JSM-IT 500 HR*) with a field emission gun (FEG) and a voltage of 5 kV, as a function of soaking time in c-SBF. Secondary electron detector (SED) was used for imaging. The elemental composition was determined by Electron dispersive X-ray Spectroscopy using an *Ultim Max 170 Oxford EDS* detector coupled to SEM. The accelerating voltage was set to 5 kV and the working distance to 10 mm.

Sample	D_{pore} (nm)	V_{pore} (cm^3/g)	S_{BET} (m^2/g)	Pore distribution
58S	14	0.42	123	Disordered
70S30C	14	0.44	109	Disordered

Table 1 Physical parameters of two types of bioactive glasses, 58S and 70S30C. D_{pore}: average pore diameter, V_{pore}: pore volume and S_{BET}: specific surface area.

2.3 *In-Vitro* bioactive tests in c-SBF

A conventional simulated body fluid (c-SBF) was used in this work for *in-vitro* tests in order to assess the bioactivity of synthesized bioglasses without using any protein and cells. The solution used for the tests, had a pH of 7.4 and was buffered with Tris(hydroxymethyl)aminomethane base (TRIS), as described elsewhere [49]. All the *in-vitro* bioactivity tests were conducted by soaking a specimen in SBF for different interaction times. (1h, 3h, 6h, 12h, 18h, 3d, and 7d) at 36.7°C with agitation speed at 70 rpm. The appropriate volume of SBF was calculated by using the following protocol described by Lukito et *al.* [50] with a powder-to-liquid-ratio = 2mg/mL. The specimens were put in a vertical position to ensure proper contact with the c-SBF liquid. After each specific interval, the specimens were extracted and washed with water and acetone to eliminate any remaining residue of SBF and stop any reactions on their surfaces.

2.4 Total X-ray Scattering

Total X-ray scattering measurements were conducted on two distinct beamlines: the Cristal beamline at Soleil synchrotron facility (E=24.0558 keV (λ=0.51495 Å)) and at the Material Science (MS) beamline at Swiss Light Source (SLS) (E=25.20 KeV (λ=0.491676 Å)). Data were collected before and after immersing two bioglasses, 58S and 70S30C, in a physiological fluid for various soaking times. The scattered intensity of the wetted samples provides information and insights on the interaction between SiO_2-SiO_2, SiO_2-Confined Species (CS) and CS-CS, as reported by Hsieh and his colleagues in 2013 [51] and applied successfully by Khoder et *al.* to the study of the structure of confined water inside the bioglasses [52]. The scattered intensity of the dry samples only shows information about the SiO_2-SiO_2 pairs. Thus, the difference intensities between the wetted and dry sample is calculated in order to isolate the contribution of different species obtained during the interactive process with the bodily fluid:

$$\boldsymbol{I = I_{wet\ sample} - I_{dry\ sample} \quad = I_{CS-CS} + I_{CS-SiO2}} \tag{1}$$

All the data processing was performed using the software PDFgetX3 [53]. The measured scattering intensity was normalized by dividing it by the average scattering factors over all the atoms and the total number of the scattering centers to obtain the scattering structure function S(Q) of each sample. Subsequently, by performing a direct sine Fourrier transform of the resulting S(Q), the experimental PDF, G(r), can be calculated in real space using the following equation:

$$\boldsymbol{G(r) = \frac{2}{\pi}\int_0^\infty Q[S(Q) - 1]\, sin(Qr)\, dQ} \tag{2}$$

To perform this calculation, data were processed by integrating and truncating them at a finite maximum of Q_{max} = *14.5* A^{-1}. Any data beyond this value was inaccurate, as the signal-to-noise ratio becomes unfavorable. Moreover, a deconvolution has been performed for all the PDFs in order to follow in detail the development of different species on the surface of the BGs. It is based on the Singular Value Decomposition (SVD) method [54], allowing for a quantitive assessment of different species that contribute to the PDFs.

2.5 Raman Spectroscopy

The Raman spectra were performed using a Reinshaw inVia Qontor spectrometer equipped with a confocal microscope and an Olympus X50 lens that has a numerical aperture (N.A.) of 0.55. A laser power range from 50 to 100 mW was used to excite all the silicate samples with a wavelength of 532 nm. All the measurements were collected in a range between 100 to 4000 cm^{-1}, with a spectral resolution of 4 cm^{-1} and a bleaching duration of 120 seconds. Ten acquisitions were performed, each one consisting of measuring the spectrum for a period of 5 seconds. Furthermore, all the probed spot areas had a size of only few micrometers squared. Multiple spots were

measured for each sample. The Raman spectra were also collected on a commercial crystalline carbonate hydroxyapatite (HCA) (Bio-Rad) and calcium carbonate powder (≥99.0%, Prolabo), in order to compare and understand the patterns observed on the BGs. The Raman spectra were decomposed using Origin software by curve fitting with Gaussian functions [55].

3. Results:

3.1 Structural Characterization

The structure and texture of the synthetic biomaterials were analyzed using nitrogen adsorption desorption techniques (**Fig. 2**.). The binary and ternary glasses isotherms correspond to type IV, as classified by IUPAC [56] suggesting a mesoporous structure. Further details regarding the structural parameters of both BGs, can be found in table 1. SEM was also used to examine the morphology for all silicate samples, displaying the presence of smooth surface for both dry BGs (**Fig. 3.**).

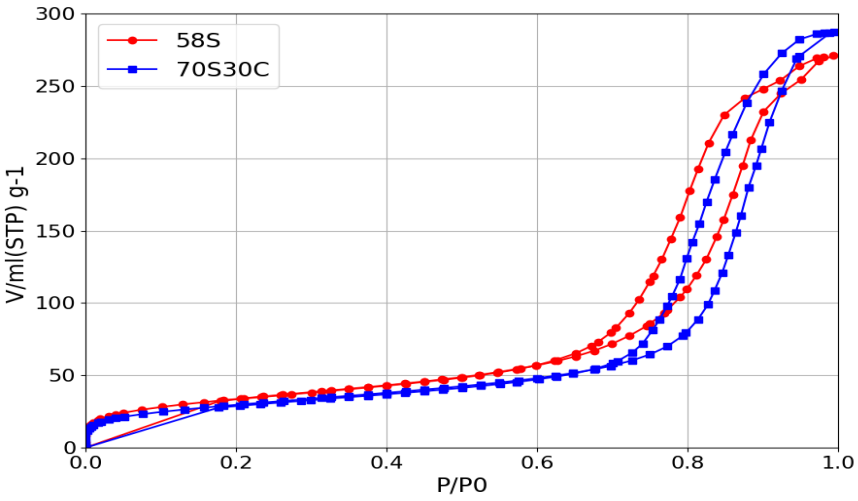

Fig. 2. Nitrogen Adsorption Desorption Isotherm of bioglasses (58S and 70S30C).

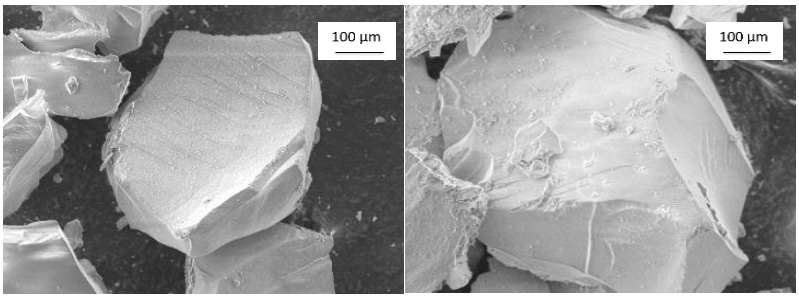

Fig. 3. SEM images of bioactive glasses, 58S (left) and 70S30C (right) before immersion in SBF.

3.2 Apatite Formation after in-Vitro Tests

Fig. 4. shows the differential PDFs (d-PDFs) of 70S30C (a) and 58S (b) bioglasses. These analyses were carried out for different immersion times in c-SBF solution. The PDFs of calcite (CC), crystalline HCA, and Calf-bones are presented as references to evaluate the bioactivity of the desired materials in the *in-vitro* experiments. Based on the PDF analysis carried on the bone and crystalline HCA, we can associate the peak at 1.5 Å with "P-O" (first neighbors), the peak at 3.6 Å to "Ca-P"or "P-O" (third neighbors) pairs, the peak at 4.1 Å to "C-P" pairs and the peak at 6.3 Å to "P-P" pairs.

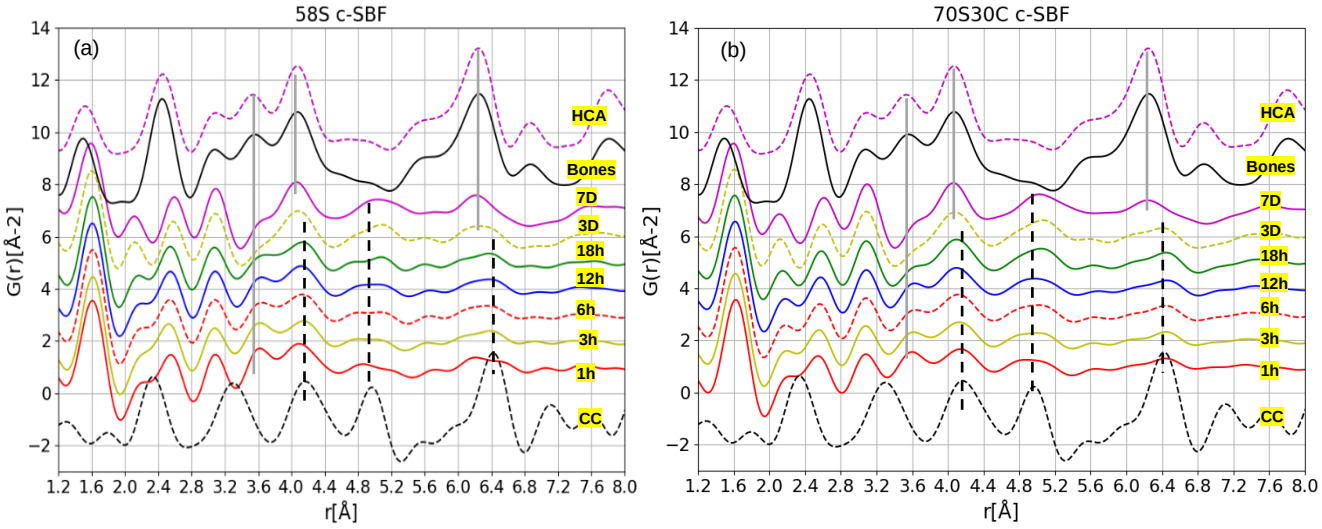

Fig. 4. Differential pair distribution functions, d-PDFs, of two types of bioglasses (70S30C (a) and 58S (b)) with different immersion times [1h (1hour), 3h, 6h, 12h, 18h, 3 days (3D), and 7 days (7D)] in c-SBF and compared to the commercial calcite (CC) and H(C)A, and the calf bones.

In the following, we will use the three peaks (3.6, 4.1 and 6.3 Å) as indicators of the presence and growth of the phosphate phases. At the earlier immersion stages of both BGs (58S and 70S30C) in the c-SBF, we can observe a main peak at 3.6 Å that could be attributed to the presence of an amorphous layer rich in calcium phosphate (ACP) or H(C)A phase. Similar features have been reported in the study of Skippers et *al.* [57].

From the PDF diagram of calcite, the first peak located at 1.27 Å can be associated with C-O pairs, while the second peak and third peaks at 2.34 and 3.34 Å correspond to mainly Ca-O and Ca-C bonds, respectively. The PDF peaks observed at 4.19 Å, 5 Å and 6.4 Å correspond to Ca-O pairs (second neighbors), Ca-Ca, and Ca-C pairs, respectively [58]. These three peaks (indicated by black dashed lines) will be used as markers for the discussion concerning the evolution of the calcite phase during the interactive process with the SBF. The formation of a calcite crystalline phase is clearly displayed in both bioglasses from the first hour, as shown in **Fig. 4**. Following the interaction for three days, these peaks have moved towards the positions of peaks corresponding to phosphate phases (indicated by grey lines). This clearly shows that both MBGs exhibit changes in their local structure, evolving towards the reference structures of bone and the crystalline HCA phase, albeit a slightly shifted peak position

(less than 0.1 Å) compared to bulk HCA. This tiny shift could suggest a slight relaxation of the structure of the confined phases within nanopores compared to bulk crystalline HCA. In fact, such relaxation has also been observed in the previous studies of confined molecules in a mesoporous silica matrix [51].

To summarize, the PDF analysis in this work indicates the presence of amorphous calcium phosphate ACP and/or H(C)A phase on both bioglasses from the initial stages of interaction with c-SBF solution. Thus, in order to confirm this hypothesis, a complementary analysis by Raman spectroscopy has been conducted.

Fig. 5 (a)(b) display the Raman spectra of 58S and 70S30C, respectively, after being soaked in conventional SBF. The spectral range considered is between 400 and 1300 cm^{-1}, which includes the main vibrational bands of silica and phosphate phases [59]. According to literature [59], the presence of crystalline carbonate hydroxyapatite (HCA) is indicated by P-O bands at 435, 590, 960, and 1075 cm^{-1} while the amorphous phase ACP is presented by broader P-O bands at 630, 950, and 1080 cm^{-1}. Thus, by examining the position and the shape of these peaks, the various phosphate phases can be distinguished. Moreover, the presence of the calcite phase can be identified through the presence of a band at 1087 cm^{-1}, which corresponds to the symmetric stretching mode of carbonate ions. In this study, for the dry binary BG (70S30C), the

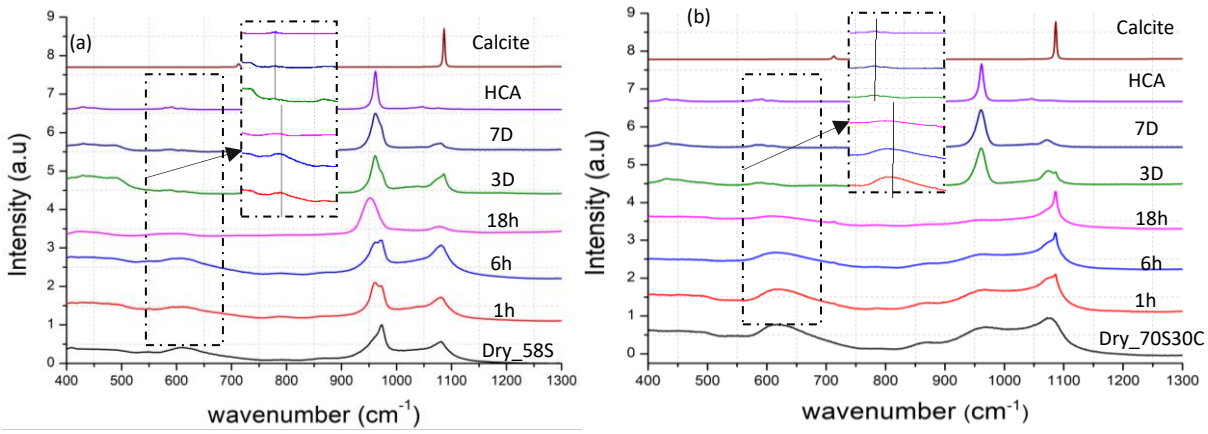

Fig. 5. Raman Spectra of BGs 58S (a) and 70S30C (b) before and after the contact with the c-SBF for different immersion durations and compared to the commercial calcite and HCA.

broad bands that are observed between 520-750, 820-1000, and between 1000-1200 cm^{-1} can be assigned to different molecular vibrations modes. For instance, the first band corresponds to the deformation mode of Si-O-Si group, the second band indicates the symmetric stretching modes of the Si-O-Si bond with different non-bridging oxygens, and the third to the asymmetric stretching of Si-O-Si fragments [60].

For the spectrum of the dry ternary BG (58S), a broad band is observed, characterized by a sharp maximum at 971 cm^{-1} and a shoulder at 957 cm^{-1}, indicative of the symmetric stretching modes of the Si-O-Si bond and PO_4^{3-} group. Additionally, a peak at 1074 cm^{-1} is associated with the antisymmetric stretching mode of PO_4^{3-}. These bands indicate thus the presence of a phosphate phase in the dry silicate BG (58S).

Upon one-hour contact of 58S BG with c-SBF (refer to **Fig. 5(a)**), the shoulder at 957 cm^{-1} transforms into a clearly visible peak at 955 cm^{-1}, that can be associated to a phosphate phase, more specifically the ACP phase. With increasing immersion time, this peak starts to move towards 960 cm^{-1}, indicating the formation of an apatite phase (H(C)A) on the surface of the ternary 58S BG. This observation is consistent with the PDF results (see **Fig. 4.**), where we were able to detect the presence of the phosphate phase from the early stages, and detect its transformation into a crystalline H(C)A phase. This crystalline phosphate phase reaches its maximum over a period of 7 days. Furthermore, the formation of calcium carbonate (calcite) starts after 1 h of contact with c-SBF and then almost disappears within one week.

In contrast, in the case of binary BG (70S30C) (**Fig. 5(b)**), the intensities of the bands associated to the vibrational modes of Si-O-Si decrease with increasing soaking times. The presence of the calcite phase was also observed in the initial stages of immersion, increasing until 18h followed by a subsequent reduction within one week. After a period of 3 days, the hydroxyapatite phase became visibly noticeable without any clear prior indication.

In order to corroborate further our findings, SEM analysis was performed on both BGs with different interaction times. Initially, the dry MBGs have a smooth texture on their surfaces (**Fig. 3.**). Upon being submerged in SBF, the surfaces begin to gradually roughen and become covered with a layer of phosphate phase and/or calcite (**Fig. 6.**). These phases have been successfully identified from the d-PDF analysis (**Fig. 6.**) after just one hour of immersion, specifically in the case of the binary glass (70S30C).

Furthermore, we performed EDS analysis on the reported areas of the **Fig. 6(b)(d)**, confirming the presence of a ratio of calcium and phosphore similar to that found in ACP and H(C)A phases. Further information on EDS analysis are given in

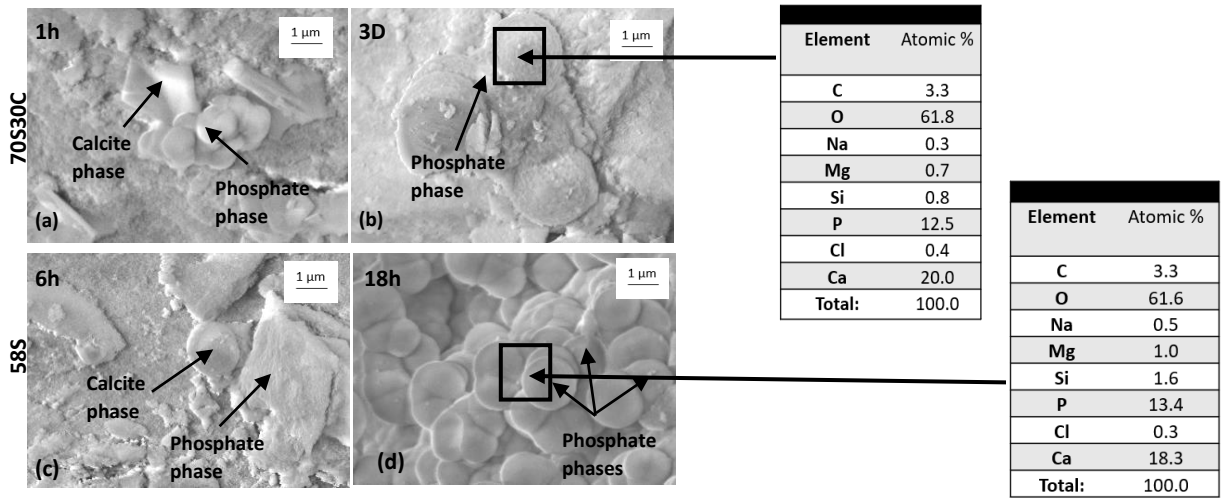

Element	Atomic %
C	3.3
O	61.8
Na	0.3
Mg	0.7
Si	0.8
P	12.5
Cl	0.4
Ca	20.0
Total:	100.0

Element	Atomic %
C	3.3
O	61.6
Na	0.5
Mg	1.0
Si	1.6
P	13.4
Cl	0.3
Ca	18.3
Total:	100.0

Fig. 6. SEM images of BGs 70S30C (a)(b) and 58S (c)(d) after being soaked in c-SBF with different immersion times. EDS analysis was done on the whole rectangle area of both images (b) and (d).

supplementary information.

4. Discussion:

In the d-PDF analysis (**Fig. 4**), we were able to track the formation of the phosphate phases from the first hour of immersion of the binary glass 70S30C (**Fig. 4(b)**), whereas the sole Raman results are not unambiguous due to the contribution of multiple phases (silica, ACP…) in the region 925-975 cm^{-1}. For further detailed analysis on the presence of the ACP phase, we performed a spectral decomposition in the region 800-1100 cm^{-1} (more details are given in Supplementary data). **Fig. 7.** presents the evolution of three phases: ACP, CC, and H(C)A from the decomposition of Raman and PDF data over different immersion times for both prototypical BGs (58S and 70S30C). The evolution of the silicate phase is given in the supplementary material. As can be seen from this figure, there is a good agreement between the deconvolution of PDF and Raman analysis when studying the formation and development of different phases on the surface of bioglasses over various soaking times. Both analyses show the same tendency in the evolution of different species in the binary (70S30C) and ternary (58S) glasses but their quantities slightly differ. This difference can be attributed to the different types of information analyzed by each technique: local information from Raman spectroscopy and global information from PDF analysis. The presence of two phases, namely amorphous calcium phosphate (ACP) and calcite (CC) phases appear immediately after the direct contact of both BGs with synthetic physiological fluid. Over a period of 18h, the ACP phase reaches the highest amount, while the H(C)A phases cannot be unambiguously detected. Subsequently, there is a notable drop in the amounts of ACP, particularly in the case of 70S30C BG, followed by a significant raise in the H(C)A phases (**Fig. 7(a)**). These findings provide a clear evidence that the ACP phase undergoes a transformation into the H(C)A phase, suggesting that ACP serves as main precursor for the nucleation of the apatite mineral phase. On the other hand, the ACP concentration in the ternary BG (58S) exhibits only a slight drop with the still significant raise in H(C)A concentration (**Fig. 7(c)(d)**). This tiny reduction of the ACP phase can be explained by the continuous formation of this amorphous phase even after a period of 3 days, due to the presence of two sources of phosphorous: the SBF solution and the BG itself (58S). However, in the binary BG (70S30C), there is only one source of phosphate (from the solution), resulting in a more significant reduction of the ACP amounts within 3 days of immersion. These insights can be considered as evidence to support the Hench's theory. According to this mechanism, the ACP phase starts to form prenucleation clusters on the surface of BGs directly after interaction with SBFs. Then, these clusters aggregate to form ACP particles, which eventually grow and transform into H(C)A phase. This has also been demonstrated in previous works [40,61], where the initial formation of ACP layer on the BGs and its subsequent crystallization after a specific duration were detected by using Small angle X-ray scattering (SAXS) and Fourier transform infrared reflection spectroscopy. Moreover, in the case of 70S30C, the calcium carbonate (CC) phase increased continuously until it reached saturation within 3 days in contact with c-SBF solution, unlike in the case of

ternary 58S BG, where there is a significant reduction of the CC phase after 18h. This difference can be explained by the presence of phosphorous in low amounts in the binary case, favorizing the formation of calcite in the available nucleation sites where they persist even after 7 days. This is a clear evidence of the presence of a competition between ACP and calcium carbonate in occupying the free nucleation sites on the BGs' surfaces. Thus, the presence of a high phosphorous amount is essential in promoting the formation of the crystalline H(C)A phase, which in the course of the reaction contribute in reducing the development of crystalline calcite phases.

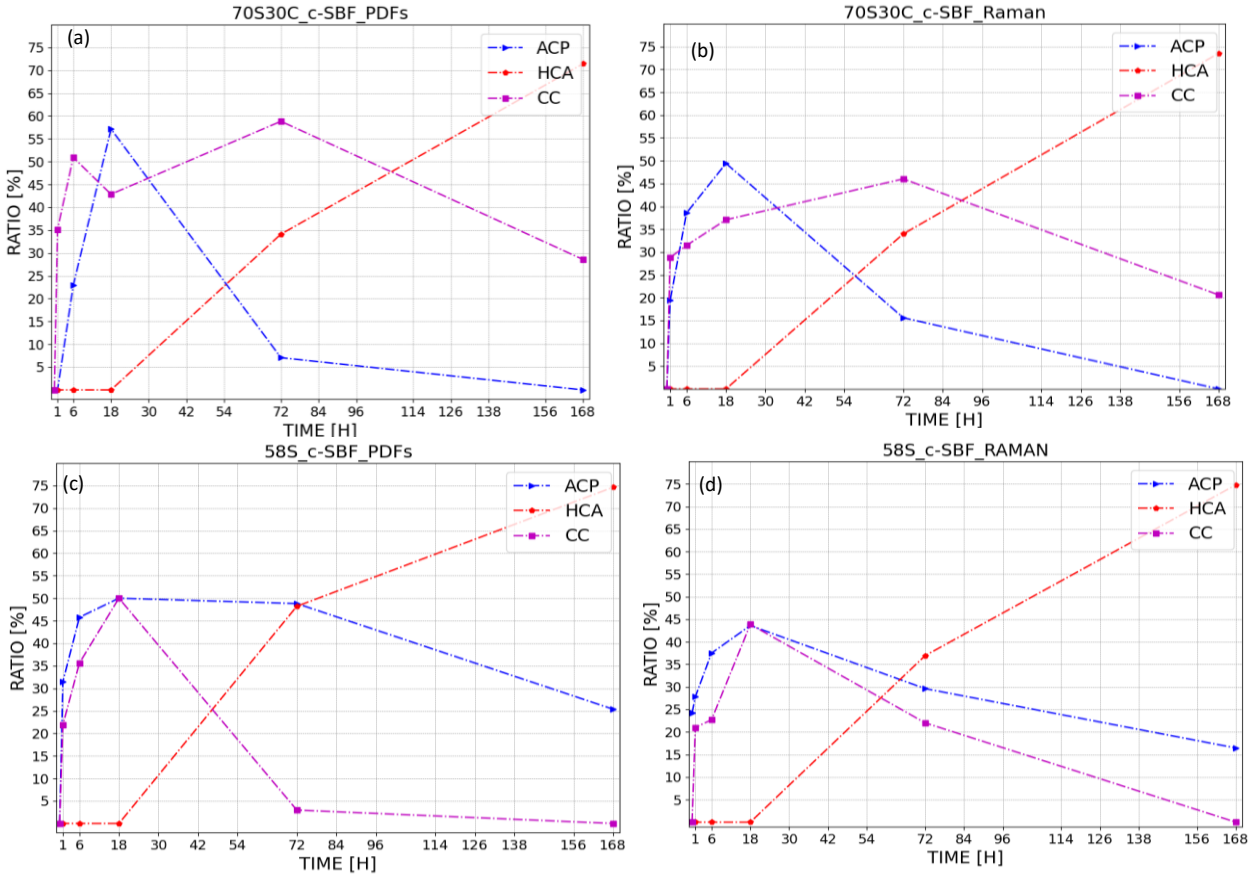

Fig. 7. The decomposition results for the PDFs of 70S30C and 58S indicated by (a) and (c) respectively. (b) and (d) represent the Raman spectra decomposition of 70S30C and 58S.

The drop of the calcite phase in the ternary glass (58S) after 18h followed by an increase of H(C)A with slight decrease of ACP, suggests a transformation of the calcite phase, possibly towards ACP, due to the incorporation of the remained phosphorous ions from the solution. This phenomenon has also been shown in the studies of Sun Yanyan et *al.* [62], where the calcite (CC) transformed into H(C)A phase through the prolonged soaking times in a phosphate solution like K_2HPO_4.

Furthermore, note that by combining these findings with the EDS analysis, we can attribute the presence of phosphate phases in the earlier stages (1h to 18h) as shown in **Fig. 6(a)(c)(d)** to the presence of amorphous ACP species and the phosphate phases in **Fig. 6(b)** to crystalline apatite (H(C)A). The presence of silicon (Si) in these areas can be attributed to the silica gel layer that precipitate under the phosphate

phases. To conclude, by referring to our previous discussion, we can confirm that the presence of smaller amounts of phosphate phases (**Fig. 6.**) on both BGs in the earlier immersion stages can be attributed to the presence of an amorphous calcium phosphate (ACP) instead of crystalline phases. So, by considering all the results, we can study the evolution of all the phases step by step from the first hour in order to evaluate the behavior of bioglasses *in-vitro* and confirming the Hench transformation path of the crystalline phosphate phases.

5. Conclusion:

In summary, by using the d-PDF analysis coupled with Raman data, we were able to monitor the evolution of the various structural phases forming on the BGs' surfaces over different immersion times. In particular, the amorphous calcium phosphate (ACP) and crystalline calcium carbonate (CC) phases were tracked in the two investigated BGs (58S and 70S30C), revealing a competition between them in the occupation of the nucleation sites followed by a gradual transformation into a mineral-like phase named H(C)A. It is also essential to highlight in this context the possibility of the transformation of CC into ACP before ultimately becoming H(C)A. Overall, our study shows that consistent quantitative information on the phases involved in H(C)A formation can be obtained from deconvoluted differential PDF and Raman spectra.

CRediT authorship contribution statement:

Amira Ghneim: Writing – original draft, Visualization, Investigation. Lea Abou Samra: Visualization, Investigation. Dominik Schaniel: Writing, Investigation. Samantha Soule: SEM and EDS measurements and analysis. Cédric Carteret: Raman Measurements. El-Eulmi Bendeif: Writing, correcting, d-PDF analysis, Investigation.

Acknowledgements:

We would like to thank Lionel Richaudeau from (L2CM) Laboratory at Lorraine University for providing a crystalline carbonate hydroxyapatite as a sample reference. We acknowledge Swiss Light Source (SLS) and Soleil for providing synchrotron radiation, and we want to thank Dr. Antonio Cervellino for the synchrotron measurements using Material Science (MS) beamline at SLS as well as Dr. Erik Elkaim for his assistance in using Cristal beamline at Soleil (*project number 20220732*).

The authors would like to thank the PMD²X X-ray diffraction facility of the CRM² laboratory (*https://crm2.univ-lorraine.fr/plateformes/pmd2x/),* Université de Lorraine, for preliminary X-ray diffraction measurements. Authors also thank the Spectroscopy and Microscopy Service Facility (SMI) of LCPME (Université de Lorraine-CNRS: *https://www.lcpme.ul.cnrs.fr/)* for the SEM-EDS and Raman analyses.

A.G. is indebted to the French Ministry of Higher Education and Research and Université de Lorraine for a doctoral fellowship.

References:

[1] L.L. Hench, R.J. Splinter, W.C. Allen, T.K. Greenlee, Bonding mechanisms at the interface of ceramic prosthetic materials, J. Biomed. Mater. Res. 5 (1971) 117–141. https://doi.org/10.1002/jbm.820050611.

[2] L.L. Hench, J. Wilson, Surface-Active Biomaterials, Science. 226 (1984) 630–636. https://doi/10.1126/science.6093253.

[3] Yamamuro Takao, Hench Larry L, Wilson June, CRC handbook of bioactive ceramics, CRC Press, Boca Raton, Fla, 1990.

[4] L.L. Hench, Bioceramics, a clinical success, Am. Ceram. Soc. Bull. 77 (1998) 67–74. https://doi.org/10.1111/j.1151-2916.1998.tb02540.x.

[5] M.N. Rahaman, R.F. Brown, B.S. Bal, D.E. Day, Bioactive glasses for nonbearing applications in total joint replacement, in: Semin. Arthroplasty, Elsevier, 2006: pp. 102–112. https://doi.org/10.1053/j.sart.2006.09.003.

[6] H.E. Skallevold, D. Rokaya, Z. Khurshid, M.S. Zafar, Bioactive glass applications in dentistry, Int. J. Mol. Sci. 20 (2019) 5960. https://doi.org/10.3390/ijms20235960.

[7] J.R. Jones, Review of bioactive glass: from Hench to hybrids, Acta Biomater. 9 (2013) 4457–4486. https://doi.org/10.3390/ijms20235960.

[8] Q.Z. Chen, I.D. Thompson, A.R. Boccaccini, 45S5 Bioglass®-derived glass–ceramic scaffolds for bone tissue engineering, Biomaterials. 27 (2006) 2414–2425. https://doi.org/10.1016/j.biomaterials.2005.11.025.

[9] L.L. Hench, J.K. West, The sol-gel process, Chem. Rev. 90 (1990) 33–72. https://doi.org/10.1021/cr00099a003.

[10] R. Li, A. Clark, L. Hench, An investigation of bioactive glass powders by sol-gel processing, J. Appl. Biomater. 2 (1991) 231–239. https://doi.org/10.1002/jab.770020403.

[11] A. El-Fiqi, T.-H. Kim, M. Kim, M. Eltohamy, J.-E. Won, E.-J. Lee, H.-W. Kim, Capacity of mesoporous bioactive glass nanoparticles to deliver therapeutic molecules, Nanoscale. 4 (2012) 7475–7488. https://doi.org/10.1039/C2NR31775C.

[12] R.A. Martin, S. Yue, J.V. Hanna, P. Lee, R.J. Newport, M.E. Smith, J.R. Jones, Characterizing the hierarchical structures of bioactive sol–gel silicate glass and hybrid scaffolds for bone regeneration, Philos. Trans. R. Soc. Math. Phys. Eng. Sci. 370 (2012) 1422–1443. https://doi.org/10.1098/rsta.2011.0308.

[13] L.L. Hench, Chronology of bioactive glass development and clinical applications, (2013). http://dx.doi.org/10.4236/njgc.2013.32011.

[14] L.L. Hench, Bioceramics: from concept to clinic, J. Am. Ceram. Soc. 74 (1991) 1487–1510. https://doi.org/10.1111/j.1151-2916.1991.tb07132.x.

[15] Y. Ebisawa, T. Kokubo, K. Ohura, T. Yamamuro, Bioactivity of CaO· SiO 2-based glasses: in vitro evaluation, J. Mater. Sci. Mater. Med. 1 (1990) 239–244. http://dx.doi.org/10.4236/njgc.2013.32011.

[16] S. Fujibayashi, M. Neo, H.-M. Kim, T. Kokubo, T. Nakamura, A comparative study between in vivo bone ingrowth and in vitro apatite formation on Na2O–CaO–SiO2 glasses, Biomaterials. 24 (2003) 1349–1356. https://doi.org/10.1016/S0142-9612(02)00511-2.

[17] M. Cerruti, Surface characterization of silicate bioceramics, Philos. Trans. R. Soc. Math. Phys. Eng. Sci. 370 (2012) 1281–1312. https://doi.org/10.1098/rsta.2011.0274.

[18] L. Skipper, F. Sowrey, R. Rashid, R. Newport, X-ray diffraction and solid state NMR studies of the, Phys. Chem. Glas. 46 (2005).

[19] C. Turdean-Ionescu, B. Stevensson, J. Grins, I. Izquierdo-Barba, A. Garcia, D. Arcos, M. Vallet-Regi, M. Edén, Composition-dependent in vitro apatite formation at mesoporous bioactive glass-surfaces quantified by solid-state NMR and powder XRD, RSC Adv. 5 (2015) 86061–86071. https://doi.org/10.1039/C5RA13410B.

[20] P.N. Gunawidjaja, I. Izquierdo-Barba, R. Mathew, K. Jansson, A. Garcia, J. Grins, D. Arcos, M. Vallet-Regi, M. Edén, Quantifying apatite formation and cation leaching from mesoporous bioactive glasses in vitro: a SEM, solid-state NMR and powder XRD study, J. Mater. Chem. 22 (2012) 7214–7223. https://doi.org/10.1039/C2JM15066B.

[21] K.S. Lin, Y.-H. Tseng, Y. Mou, Y.-C. Hsu, C.-M. Yang, J.C. Chan, Mechanistic study of apatite formation on bioactive glass surface using 31P solid-state NMR spectroscopy, Chem. Mater. 17 (2005) 4493–4501. https://doi.org/10.1021/cm050654c.

[22] S. Hayakawa, K. Tsuru, C. Ohtsuki, A. Osaka, Mechanism of apatite formation on a sodium silicate glass in a simulated body fluid, J. Am. Ceram. Soc. 82 (1999) 2155–2160. https://doi.org/10.1111/j.1151-2916.1999.tb02056.x.

[23] E. Dietrich, H. Oudadesse, M. Le Floch, B. Bureau, T. Gloriant, In vitro Chemical Reactivity of Doped Bioactive Glasses: an Original Approach by Solid-State NMR Spectroscopy, Adv. Eng. Mater. 11 (2009) B98–B105. https://doi.org/10.1002/adem.200800400.

[24] P.N. Gunawidjaja, A.Y. Lo, I. Izquierdo-Barba, A. Garcia, D. Arcos, B. Stevensson, J. Grins, M. Vallet-Regi, M. Edén, Biomimetic apatite mineralization mechanisms of mesoporous bioactive glasses as probed by multinuclear ^{31}P, ^{29}Si, ^{23}Na and ^{13}C solid-state NMR, J. Phys. Chem. C. 114 (2010) 19345–19356. https://doi.org/10.1021/jp105408c.

[25] P.N. Gunawidjaja, R. Mathew, A.Y. Lo, I. Izquierdo-Barba, A. García, D. Arcos, M. Vallet-Regí, M. Edén, Local structures of mesoporous bioactive glasses and their surface alterations in vitro: inferences from solid-state nuclear magnetic resonance,

Philos. Trans. R. Soc. Math. Phys. Eng. Sci. 370 (2012) 1376–1399. https://doi.org/10.1098/rsta.2011.0257.

[26] R. Mathew, P.N. Gunawidjaja, I. Izquierdo-Barba, K. Jansson, A. García, D. Arcos, M. Vallet-Regí, M. Edén, Solid-state 31P and 1H NMR investigations of amorphous and crystalline calcium phosphates grown biomimetically from a mesoporous bioactive glass, J. Phys. Chem. C. 115 (2011) 20572–20582. https://doi.org/10.1021/jp206237n.

[27] X. Yan, C. Yu, X. Zhou, J. Tang, D. Zhao, Highly ordered mesoporous bioactive glasses with superior in vitro bone-forming bioactivities, Angew. Chem. Int. Ed. 43 (2004) 5980–5984. https://doi.org/10.1002/anie.200460598.

[28] X. Yan, X. Huang, C. Yu, H. Deng, Y. Wang, Z. Zhang, S. Qiao, G. Lu, D. Zhao, The in-vitro bioactivity of mesoporous bioactive glasses, Biomaterials. 27 (2006) 3396–3403. https://doi.org/10.1016/j.biomaterials.2006.01.043.

[29] A. López-Noriega, D. Arcos, I. Izquierdo-Barba, Y. Sakamoto, O. Terasaki, M. Vallet-Regí, Ordered mesoporous bioactive glasses for bone tissue regeneration, Chem. Mater. 18 (2006) 3137–3144. https://doi.org/10.1021/cm060488o.

[30] I. Izquierdo-Barba, D. Arcos, Y. Sakamoto, O. Terasaki, A. López-Noriega, M. Vallet-Regí, High-performance mesoporous bioceramics mimicking bone mineralization, Chem. Mater. 20 (2008) 3191–3198. https://doi.org/10.1021/cm800172x.

[31] A. García, M. Cicuéndez, I. Izquierdo-Barba, D. Arcos, M. Vallet-Regí, Essential role of calcium phosphate heterogeneities in 2D-hexagonal and 3D-cubic SiO2- CaO-P2O5 mesoporous bioactive glasses, Chem. Mater. 21 (2009) 5474–5484. https://doi.org/10.1021/cm9022776.

[32] H. Takadama, H.-M. Kim, T. Kokubo, T. Nakamura, Mechanism of biomineralization of apatite on a sodium silicate glass: TEM- EDX study in vitro, Chem. Mater. 13 (2001) 1108–1113. https://doi.org/10.1021/cm0008718.

[33] C. Berbecaru, G. Stan, S. Pina, D. Tulyaganov, J. Ferreira, The bioactivity mechanism of magnetron sputtered bioglass thin films, Appl. Surf. Sci. 258 (2012) 9840–9848. https://doi.org/10.1016/j.apsusc.2012.06.039.

[34] F. Branda, R. Fresa, A. Costantini, A. Buri, Bioactivity of 1.25 CaO· SiO2 glass: an FTIR and X-ray study on powdered samples, Biomaterials. 17 (1996) 2247–2251. https://doi.org/10.1016/0142-9612(95)00328-2.

[35] A. Salinas, A. Martin, M. Vallet-Regí, Bioactivity of three CaO–P2O5–SiO2 sol-gel glasses, J. Biomed. Mater. Res. Off. J. Soc. Biomater. Jpn. Soc. Biomater. Aust. Soc. Biomater. Korean Soc. Biomater. 61 (2002) 524–532. https://doi.org/10.1002/jbm.10229.

[36] M. Cerruti, C.L. Bianchi, F. Bonino, A. Damin, A. Perardi, C. Morterra, Surface modifications of bioglass immersed in TRIS-buffered solution. A multitechnical spectroscopic study, J. Phys. Chem. B. 109 (2005) 14496–14505. https://doi.org/10.1021/jp050705t.

[37] J. Lao, J.-M. Nedelec, E. Jallot, New Insight into the Physicochemistry at the Interface between Sol- Gel-Derived Bioactive Glasses and Biological Medium: A PIXE-RBS Study, J. Phys. Chem. C. 112 (2008) 9418–9427. https://doi.org/10.1021/jp800583m.

[38] J. Soulié, J. Lao, E. Jallot, J.-M. Nedelec, Influence of mesostructuration on the reactivity of bioactive glasses in biological medium: a PIXE-RBS study, J. Mater. Chem. 22 (2012) 20680–20688. https://doi.org/10.1039/C2JM30880K.

[39] R. Li, A. Clark, L. Hench, An investigation of bioactive glass powders by sol-gel processing, J. Appl. Biomater. 2 (1991) 231–239. https://doi.org/10.1002/jab.770020403.

[40] C.Y. Kim, A.E. Clark, L.L. Hench, Early stages of calcium-phosphate layer formation in bioglasses, J. Non-Cryst. Solids. 113 (1989) 195–202. https://doi.org/10.1016/0022-3093(89)90011-2. [41] Ö. Andersson, I. Kangasniemi, Calcium phosphate formation at the surface of bioactive glass in vitro, J. Biomed. Mater. Res. 25 (1991) 1019–1030. https://doi.org/10.1002/jbm.820250808.

[42] M. Brink, T. Turunen, R.-P. Happonen, A. Yli-Urpo, Compositional dependence of bioactivity of glasses in the system Na2O-K2O-MgO-CaO-B2O3-P2O5-SiO2, J. Biomed. Mater. Res. Off. J. Soc. Biomater. Jpn. Soc. Biomater. 37 (1997) 114–121. https://doi.org/10.1002/(SICI)1097-4636(199710)37:1%3C114::AID-JBM14%3E3.0.CO;2-G.

[43] L. Varila, S. Fagerlund, T. Lehtonen, J. Tuominen, L. Hupa, Surface reactions of bioactive glasses in buffered solutions, J. Eur. Ceram. Soc. 32 (2012) 2757–2763. https://doi.org/10.1016/j.jeurceramsoc.2012.01.025.

[44] V. Banchet, E. Jallot, J. Michel, L. Wortham, D. Laurent-Maquin, G. Balossier, X-ray microanalysis in STEM of short-term physicochemical reactions at bioactive glass particle/biological fluid interface. Determination of O/Si atomic ratios, Surf. Interface Anal. Int. J. Devoted Dev. Appl. Tech. Anal. Surf. Interfaces Thin Films. 36 (2004) 658–665. https://doi.org/10.1002/sia.1916.

[45] M. Cerruti, A. Perardi, G. Cerrato, C. Morterra, Formation of a nanostructured layer on bioglass particles of different sizes immersed in tris-buffered solution. N2 adsorption and HR-TEM/EDS analysis, Langmuir. 21 (2005) 9327–9333. https://doi.org/10.1021/la051221r.

[46] H. Aguiar, E. Solla, J. Serra, P. González, B. León, F. Malz, C. Jäger, Raman and NMR study of bioactive Na2O–MgO–CaO–P2O5–SiO2 glasses, J. Non-Cryst. Solids. 354 (2008) 5004–5008. https://doi.org/10.1016/j.jnoncrysol.2008.07.033.

[47] V. Fitzgerald, K.O. Drake, J.R. Jones, M.E. Smith, V. Honkimäki, T. Buslaps, M. Kretzschmer, R.J. Newport, In situ high-energy X-ray diffraction study of a bioactive calcium silicate foam immersed in simulated body fluid, J. Synchrotron Radiat. 14 (2007) 492–499. https://doi.org/10.1107/S0909049507042173.

[48] T.H. Dang, T.H. Bui, E.V. Guseva, A.T. Ta, A.T. Nguyen, T.T.H. Hoang, X.V. Bui, Characterization of bioactive glass synthesized by sol-gel process in hot water, Crystals. 10 (2020) 529. https://doi.org/10.3390/cryst10060529.

[49] A. Oyane, H.-M. Kim, T. Furuya, T. Kokubo, T. Miyazaki, T. Nakamura, Preparation and assessment of revised simulated body fluids, J. Biomed. Mater. Res. Part Off. J. Soc. Biomater. Jpn. Soc. Biomater. Aust. Soc. Biomater. Korean Soc. Biomater. 65 (2003) 188–195. https://doi.org/10.1002/jbm.a.10482.

[50] D. Lukito, J. Xue, J. Wang, In vitro bioactivity assessment of 70 (wt.)% SiO2–30 (wt.)% CaO bioactive glasses in simulated body fluid, Mater. Lett. 59 (2005) 3267–3271. https://doi.org/10.1016/j.matlet.2005.05.055.

[51] K.-Y. Hsieh, E.-E. Bendeif, A. Gansmuller, S. Pillet, T. Woike, D. Schaniel, Structure and dynamics of guest molecules confined in a mesoporous silica matrix: Complementary NMR and PDF characterisation, RSC Adv. 3 (2013) 26132–26141. https://doi.org/10.1039/C3RA45347B.

[52] H. Khoder, D. Schaniel, S. Pillet, E.-E. Bendeif, X-ray scattering study of water confined in bioactive glasses: experimental and simulated pair distribution function, Acta Crystallogr. Sect. Found. Adv. 76 (2020) 589–599. https://doi.org/10.1107/S2053273320007834/vk5044sup1.pdf.

[53] P. Juhás, T. Davis, C.L. Farrow, S.J. Billinge, PDFgetX3: a rapid and highly automatable program for processing powder diffraction data into total scattering pair distribution functions, J. Appl. Crystallogr. 46 (2013) 560–566. https://doi.org/10.1107/S0021889813005190.

[54] E. Henry, J. Hofrichter, [8] Singular value decomposition: Application to analysis of experimental data, in: Methods Enzymol., Elsevier, 1992: pp. 129–192. https://doi.org/10.1016/0076-6879(92)10010-B.

[55] I. Hammami, S.R. Gavinho, A.S. Pádua, M. do C. Lança, J.P. Borges, J.C. Silva, I. Sá-Nogueira, S.K. Jakka, M.P.F. Graça, Extensive Investigation on the Effect of Niobium Insertion on the Physical and Biological Properties of 45S5 Bioactive Glass for Dental Implant, Int. J. Mol. Sci. 24 (2023) 5244. https://doi.org/10.3390/ijms24065244.

[56] M. Thommes, K. Kaneko, A.V. Neimark, J.P. Olivier, F. Rodriguez-Reinoso, J. Rouquerol, K.S. Sing, Physisorption of gases, with special reference to the evaluation of surface area and pore size distribution (IUPAC Technical Report), Pure Appl. Chem. 87 (2015) 1051–1069. https://doi.org/10.1515/pac-2014-1117.

[57] L.J. Skipper, F.E. Sowrey, D.M. Pickup, K.O. Drake, M.E. Smith, P. Saravanapavan, L.L. Hench, R.J. Newport, The structure of a bioactive calcia–silica sol–gel glass, J. Mater. Chem. 15 (2005) 2369–2374. https://doi.org/10.1039/B501496D.

[58] S.M. Clark, B. Colas, D.E. Jacob, J.C. Neuefeind, H.-W. Wang, K.L. Page, A.K. Soper, P.I. Schodder, P. Duchstein, B.A. Zubiri, others, The nano-and meso-scale

structure of amorphous calcium carbonate, Sci. Rep. 12 (2022) 6870. https://doi.org/10.1038/s41598-022-10627-9.

[59] G. Sauer, W. Zunic, J. Durig, R. Wuthier, Fourier transform Raman spectroscopy of synthetic and biological calcium phosphates, Calcif. Tissue Int. 54 (1994) 414–420. https://doi.org/10.1007/BF00305529.

[60] D. Bellucci, G. Bolelli, V. Cannillo, A. Cattini, A. Sola, In situ Raman spectroscopy investigation of bioactive glass reactivity: Simulated body fluid solution vs TRIS-buffered solution, Mater. Charact. 62 (2011) 1021–1028. https://doi.org/10.1016/j.matchar.2011.07.008.

[61] R.A. Martin, H. Twyman, D. Qiu, J.C. Knowles, R.J. Newport, A study of the formation of amorphous calcium phosphate and hydroxyapatite on melt quenched Bioglass® using surface sensitive shallow angle X-ray diffraction, J. Mater. Sci. Mater. Med. 20 (2009) 883–888. https://doi.org/10.1007/s10856-008-3661-5.

[62] S. Yanyan, W. Guangxin, L. Wuhui, W. Yaming, S. Hayakawa, A. Osaka, Conversion of sub-μm calcium carbonate (calcite) particles to hollow hydroxyapatite agglomerates in K2HPO4 solutions, Nanotechnol. Rev. 9 (2020) 945–960. https://doi.org/10.1515/ntrev-2020-0070.

Multiscale Investigation on the Formation Path of the Apatite Phase in Bioactive Glasses

GHNEIM Amira[a,1], ABOU SAMRA Lea[a,2], SCHANIEL Dominik[a,3], SOULE Samantha[b,1], CARTERET Cédric[b,2] & BENDEIF El-Eulmi [a,4]*

[a]University of Lorraine, CNRS, CRM2, UMR 7036, 54506 Vandoeuvre-lès-Nancy cedex, France

[a,1]*amira.ghneim@univ-lorraine.fr,* [a,2]*lea.abou-samra5@etu.univ-lorraine.fr,* [a, 3]*dominik.schaniel@univ-lorraine.fr,* [a,4]*el-eulmi.bendeif@univ-lorraine.fr*

[b]University of Lorraine, CNRS, LCPME, UMR 7564, 54600 Villers-lès-Nancy, France

[b,1]*samantha.soule@univ-lorraine.fr,* [b,2]*cedric.carteret@univ-lorraine.fr*

*Corresponding author : Laboratoire CRM² (UMR-CNRS 7036), Faculté des Sciences et Technologies, BP 70239, Campus, Bd des Aiguillettes, 54506 Vandoeuvre les Nancy, Cedex, France.
Tel:+33(0)372745634, Fax: +33(0)372745218
E-mail: el-eulmi.bendeif@univ-lorraine.fr

Abstract: Mesoporous bioactive glasses (MBGs) have been reported as promising biomaterials to stimulate and promote the growth of bones. When exposed to Simulated Body Fluid (SBF), MBGs develop an apatite phase called carbonate hydroxyapatite H(C)A on their surfaces that closely mimics the mineral phase of bones. In order to gain deeper insights into the key stages of the surface reactions of two different types of MBGs (58S and 70S30C) soaked in SBF, we have used high energy total X-ray scattering coupled to Pair Distribution Function (PDF) analysis, along with Raman spectroscopy and scanning electron microscopy. This type of coupled analytical approach can ultimately help to unravel the details of the reaction kinetics in the complex calcium phosphate environment around the BGs surfaces. The data obtained in our in-vitro study point to the formation of other intermediate phases like amorphous calcium phosphate (ACP) and calcite (CC), that transform after a specific time into H(C)A depending on the composition of the MBGs, their surface properties and their interaction times with SBF.

Keywords: Bioactive Glasses, Total X-ray scattering, Raman spectroscopy, Carbonate-Hydroxyapatite, Amorphous Calcium Phosphate.

1. Introduction

Since their discovery in 1969 by Hench [1], the bioactive glasses (BGs) have gone a long way in investigations. Nowadays, they are used in some applications relying on bone regeneration and tissue engineering such as filling cavities and dental, maxillofacial, and orthopedic surgery [2-7]. However, they still suffer from some drawbacks such as comparatively lower mechanical stability or other unwanted effects such as crystallization during sintering [8], that could be overcome by a detailed understanding of how the glass composition affects the crystallization [9] or by exploiting the tremendous possibilities offered by the sol-gel synthesis of BGs [10,11]. While the sol-gel process offers a high flexibility for functionalizing the porous BGs for various purposes, including drug delivery [12-13], the complexity of these materials requires multi-technique approaches to investigate the key steps in the bone-building

process. In the last decades a plethora of methods has been used to assess the bioactivity, i.e. the ability of the bioglass to bond to bone tissue and have helped to understand the key steps of the BG reaction mechanism after being exposed to simulated body fluid (SBF) in *in-vitro* experiments [14]. This mechanism, first proposed by Hench [15], can be summarized as follows (**Fig. 1.**) [16-18]:

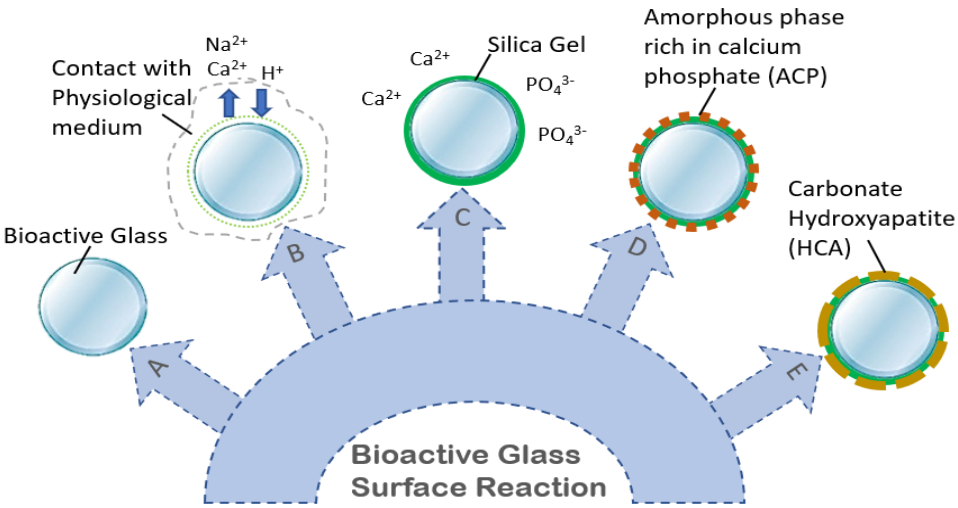

Fig. 1. Schematic representation of the first five steps of the bioactivity process of the bioactive glass as outlined by Hench [15].

The first two steps (Stage A & B) consist in a rapid cation exchange of Na^+ and/or Ca^{2+} with H^+ from solution, creating silanol bonds (Si–OH) on the glass surface. The pH of the solution increases and a silica-rich (cation-depleted) region forms near to the glass surface. Phosphates can also be lost from the glass if they are present in the composition. Furthermore, the high local pH contributes in breaking Si–O–Si bonds, by attacking the silica glass network by OH. Soluble silica is lost in the form of $Si(OH)_4$ toward the solution, leaving more Si–OH (silanols) at the glass–solution interface. In the third step (Stage C), the Si–OH groups near the glass surface condense, resulting in a repolymerization of the silica-rich layer. The fourth step (Stage D) involves the migration of Ca^{2+} and PO_4^{3-} groups from the BG itself and the bodily fluid, leading to the formation of an amorphous film rich in $CaO–P_2O_5$ on the silica-rich layer. Finally, by referring to Stage E, the incorporation of hydroxyls and carbonate ions from solution contribute to the crystallization of the $CaO–P_2O_5$ film, resulting in carbonate hydroxyapatite H(C)A formation ($Ca_{10}(PO_4)_{6-x}(CO_3)_x(OH)_2$).

As outlined, e.g., in Cerruti's review [19], these different steps have been investigated by several analytical techniques in order to further explore and study the compositions and developments of silica gel and the different phosphate phases. For instance, Solid-State multinuclear magnetic resonance (NMR) [20-28], various spectroscopies like Raman and Fourier transform infrared [17, 29-38], X-ray photo-electron [39], particle-induced X-ray emission [40,41], X-ray diffraction (XRD) [17,20-22,35,36,42,43] as well as scanning electron microscopy coupled with Electron dispersive X-ray Spectroscopy

[22,29-35,37,44-50] have been used for these investigations in order to support and validate the theory of Hench.

However, as also recently outlined in a critical review by Eden [51] concerning the structure and formation of amorphous calcium phosphate, there are still some unresolved issues and in particular the different length and time scales involved in the formation of the H(C)A phase pose a constant challenge on the overall characterization of the bioactivity of BGs. To overcome this challenge, an advanced in-situ total X-ray scattering technique coupled to PDF analysis has been developed by FitzGerald and co-workers [52] to understand the atomic structure of the complex amorphous bioactive materials and study their interactions with a physiological medium. This type of method could push the boundaries of a detailed structural characterization and understanding of the reaction mechanism even further in complement to the hitherto predominantly used analytical methods. Thus, in order to obtain quantitative information on the different species that appear during the H(C)A formation, we propose to use a differential PDF (d-PDF) approach along with a singular value decomposition (SVD) analysis. Moreover, Raman spectroscopy and scanning electron microscopy coupled to EDS are employed as complementary techniques to corroborate the findings of the total scattering study. We focused on two different prototypic bioactive glasses: 58S and 70S30C in order to gain a comprehensive understanding on the different stages of the formation of carbonate hydroxyapatite and shed light on their structural changes that occur on the atomic level. Both BGs have predominantly amorphous structure, which makes it easier to track the formation and development of any phases on their surfaces once they are immersed in SBF. By performing a quantitative analysis of the evolution of the different phases after immersion in SBF based on a combination of differential PDF analysis and Raman spectroscopy, our work might serve as a methodological reference for future studies, allowing for structural characterization of the BGs on several length scales and in particular enabling the monitoring of the evolution of amorphous phases, that are critical in the H(C)A formation. In addition, the formation of calcium carbonate in in-vitro bioactivity tests is also a matter of debate, as recently reviewed by Mozafari et al [53], and need thus to be critically assessed.

2. Materials and Methods:

2.1 Sol-Gel Synthesis

Two types of bioactive glasses, namely 70S30C (70% SiO_2, 30% CaO (mol. %)) and 58S (60% SiO_2, 36% CaO, 4% P_2O_5 (mol. %)), were synthesized through the standard sol-gel method. The main precursors used were tetraethyl orthosilicate (TEOS) (≥98.0%, Acros Organics), and calcium nitrate tetrahydrate ($Ca(NO_3)_2.4H_2O$) (CaN) (≥97.0%, Thermo Scientific). Triethyl phosphate (TEP) (≥99.8%, Sigma-Aldrich) was also used in the case of the ternary glass 58S. Initially, distilled water was stirred magnetically at either 60°C or room temperature to prepare binary and ternary bioglasses, respectively. Then, 9.33 g of TEOS and/or 0.7144g of TEP were added dropwise to the mixture and stirred until a clear solution was obtained. The molar ratio between the distilled water and the TEOS precursor was fixed at 8 and a few drops of an acidic solution were added to ensure complete hydrolysis of the silicate precursor.

The $Ca(NO_3)_2.4H_2O$ powder was slowly added to the solution and stirred until a gel was formed. Subsequently, for 58S, the gel was aged at 60°C for 55 h, dried at 180°C for 72 h, and then calcinated at 700°C for 3 h. While for 70S30C, the aging, the drying, and calcination processes were followed according to the protocol reported in [54].

2.2 Characterization of BGs

Nitrogen adsorption desorption measurements were conducted on a *Microtrac-BELSROP-Max* instrument at 77K in order to determine the structural textures of all samples (refer to **Table 1**). The specific surface area for the BGs were determined by the *Brunauer-Emmett-Teller* (BET) method while the *Barret-Joyner-Halanda* (BJH) method was used to determine the pore sizes and volumes of the BGs from the desorption curves. Prior to the analysis the samples were kept under vacuum for an hour to re-degas. The surface morphology of the bioglasses was also investigated using scanning electron microscopy (SEM) (*JEOL JSM-IT 500 HR*) with a field emission gun (FEG) and a voltage of 5 kV, as a function of soaking time in c-SBF. A secondary electron detector (SED) was used for imaging. The elemental composition was determined by Electron dispersive X-ray Spectroscopy using an *Ultim Max 170 Oxford EDS* detector coupled to SEM. The accelerating voltage was set to 5 kV and the working distance to 10 mm.

Sample	D_{pore} (nm)	V_{pore} (cm^3/g)	S_{BET} (m^2/g)	Pore distribution
58S	14	0.42	123	Disordered
70S30C	14	0.44	109	Disordered

Table 1 Physical parameters of two types of bioactive glasses, 58S and 70S30C. D_{pore}: average pore diameter, V_{pore}: pore volume and S_{BET}: specific surface area.

2.3 *In-Vitro* bioactive tests in c-SBF

A conventional simulated body fluid (c-SBF) was used in this work for *in-vitro* tests in order to assess the bioactivity of the synthesized bioglasses without using any protein and cells. The solution used for the tests had a pH of 7.4 and was buffered with Tris(hydroxymethyl)aminomethane base (TRIS), as described elsewhere [55]. All the *in-vitro* bioactivity tests were conducted by soaking a specimen in SBF for different interaction times (1h, 3h, 6h, 12h, 18h, 3d, and 7d) at 36.7°C with with magnetic stirring at 70 rpm. The appropriate volume of SBF was calculated by using the protocol described by Lukito et *al.* [56] with a powder-to-liquid-ratio = 2mg/mL. The specimens were put in a vertical position to ensure proper contact with the c-SBF liquid. After having reached the desired interaction time, the specimens were extracted and washed with water and acetone to eliminate any remaining residue of SBF and stop any reactions on their surfaces.

2.4 Total X-ray Scattering

Total X-ray scattering measurements were conducted on two distinct beamlines: the Cristal beamline at the SOLEIL synchrotron facility (E=24.0558 keV (λ=0.51495 Å)) and at the Material Science (MS) beamline at the Swiss Light Source (SLS) (E=25.20 KeV (λ=0.491676 Å)). Data were collected before and after immersing two bioglasses, 58S and 70S30C, in a physiological fluid for various soaking times. The scattered intensity of the wetted samples provides information and insights on the interaction between SiO_2-SiO_2, SiO_2-Confined Species (CS) and CS-CS, as reported by Hsieh et *al.* in 2013 [57] and applied successfully by Khoder et *al.* to the study of the structure of confined water inside the bioglasses [58]. The scattered intensity of the dry samples only shows information about the SiO_2-SiO_2 pairs. Thus, the difference of the scattering intensities between the wetted and dry sample is calculated in order to isolate the contribution of different species obtained during the interactive process with the bodily fluid:

$$\boldsymbol{I = I_{wet\ sample} - I_{dry\ sample} \quad = I_{CS-CS} + I_{CS-SiO2}} \tag{1}$$

All the data processing was performed using the software PDFgetX3 [59]. The measured scattering intensity was normalized by dividing it by the average scattering factors over all the atoms and the total number of the scattering centers to obtain the scattering structure function S(Q) of each sample. Subsequently, by performing a direct sine Fourrier transform of the resulting S(Q), the experimental PDF, G(r), can be calculated in real space using the following equation:

$$\boldsymbol{G(r) = \frac{2}{\pi}\int_0^\infty Q[S(Q) - 1]\, sin(Qr)\, dQ} \tag{2}$$

To perform this calculation, data were processed by integrating and truncating them at a finite maximum of Q_{max} = *14.5* A^{-1}. Any data beyond this value was inaccurate, as the signal-to-noise ratio becomes unfavorable. Moreover, a deconvolution has been performed for all the PDFs in order to follow in detail the development of different species on the surface of the BGs. It is based on the Singular Value Decomposition (SVD) method [60], allowing for a quantitative assessment of different species that contribute to the PDFs.

2.5 Raman Spectroscopy

The Raman spectra were collected using a Reinshaw inVia Qontor spectrometer equipped with a confocal microscope and an Olympus X50 lens that has a numerical aperture (N.A.) of 0.55. A laser power range from 50 to 100 mW was used to excite all the silicate samples with a wavelength of 532 nm. All the measurements were collected in a range between 100 to 4000 cm^{-1}, with a spectral resolution of 4 cm^{-1} and a bleaching duration of 120 seconds. Ten acquisitions were performed, each one

consisting of measuring the spectrum for a period of 5 seconds. Furthermore, all the probed spot areas had a size of only few micrometers squared. Multiple spots were measured for each sample. The Raman spectra were also collected on a commercial crystalline carbonate hydroxyapatite (HCA) (Bio-Rad) and calcium carbonate powder (≥99.0%, Prolabo), in order to compare and understand the patterns observed on the BGs. The Raman spectra were decomposed using Origin software by curve fitting with Gaussian functions [61].

3. Results:

3.1 Structural Characterization

The structure and texture of the synthetic biomaterials were analyzed using nitrogen adsorption desorption techniques (**Fig. 2**.). The binary and ternary glasses isotherms correspond to type IV, as classified by IUPAC [62] suggesting a mesoporous structure. Further details regarding the structural parameters of both BGs, can be found in table 1. SEM was used to examine the morphology for all silicate samples, demonstrating the presence of a smooth surface for both dry BGs (**Fig. 3.**).

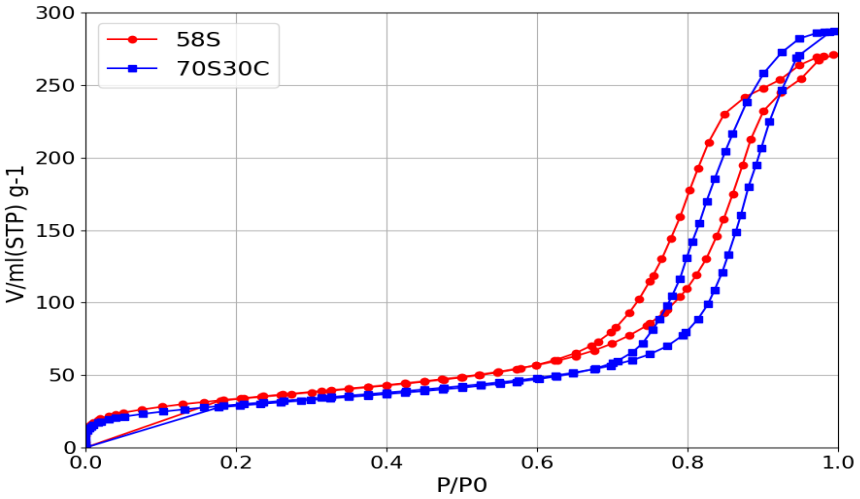

Fig. 2. Nitrogen Adsorption Desorption Isotherm of bioglasses (58S and 70S30C).

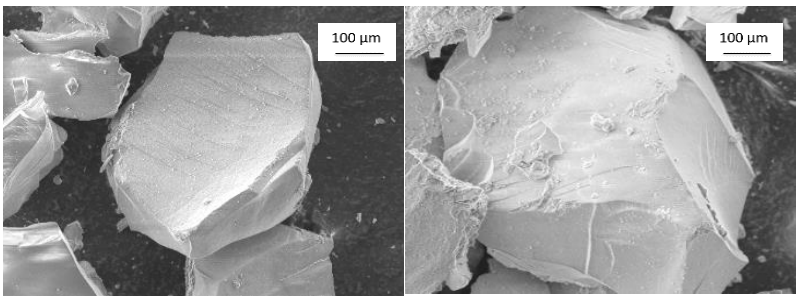

Fig. 3. SEM images of bioactive glasses, 58S (left) and 70S30C (right) before immersion in SBF.

3.2 Apatite Formation after in-Vitro Tests

Fig. 4. shows the differential PDFs (d-PDFs) of 70S30C (a) and 58S (b) bioglasses. These analyses were carried out for different immersion times in c-SBF solution. The PDFs of calcite (CC), crystalline HCA, and Calf-bones are presented as references to evaluate the bioactivity of the prepared materials in the *in-vitro* experiments. Based on

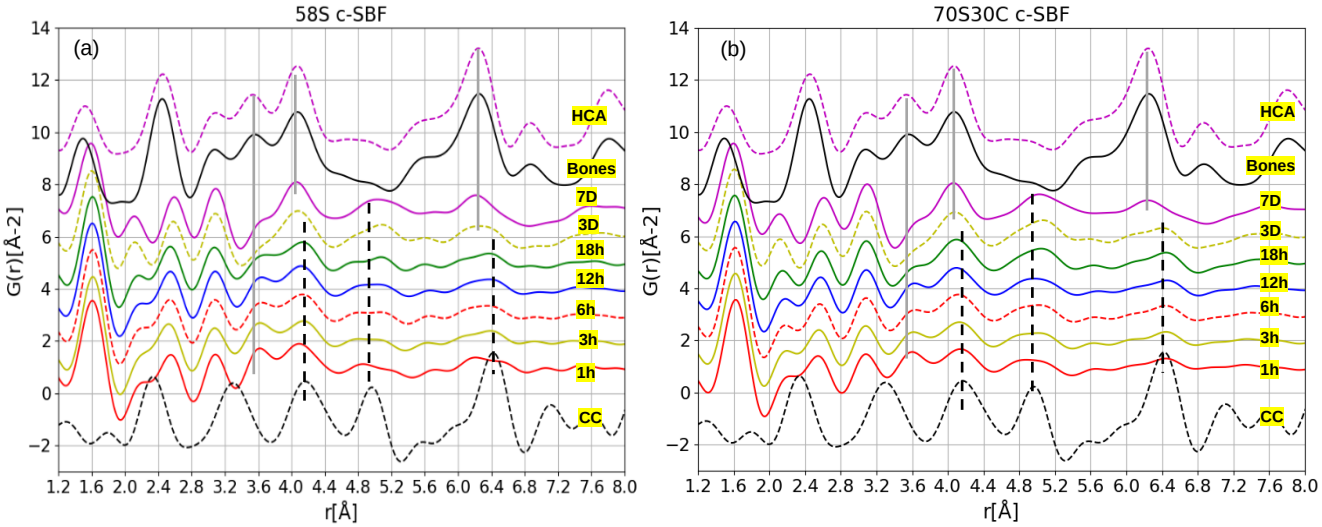

Fig. 4. Differential pair distribution functions, d-PDFs, of two types of bioglasses (70S30C (a) and 58S (b)) with different immersion times [1h (1hour), 3h, 6h, 12h, 18h, 3 days (3D), and 7 days (7D)] in c-SBF and compared to the commercial calcite (CC) and H(C)A, and the calf bones.

the PDF analysis carried on the bone and crystalline HCA, we can associate the peak at 1.5 Å with “P-O” (first neighbors) pairs, the peak at 3.6 Å with “Ca-P” or “P-O” (third neighbors) pairs, the peak at 4.1 Å with “C-P” pairs and the peak at 6.3 Å with “P-P” pairs. In the following, we will use the three peaks at 3.6, 4.1 and 6.3 Å as indicators of the presence and growth of the phosphate phases. At the earlier immersion stages of both BGs (58S and 70S30C) in the c-SBF, we can observe a main peak at 3.6 Å that could be attributed to the presence of an amorphous layer rich in calcium phosphate (ACP) or H(C)A phase. Similar features have been reported in the study of Skippers et *al.* [63].

From the PDF diagram of calcite, the first peak located at 1.27 Å can be associated with C-O pairs, while the second peak and third peaks at 2.34 and 3.34 Å correspond to mainly Ca-O and Ca-C bonds, respectively. The PDF peaks observed at 4.19 Å, 5 Å and 6.4 Å correspond to Ca-O pairs (second neighbors), Ca-Ca, and Ca-C pairs, respectively [64]. These three peaks (indicated by black dashed lines) will be used as markers for the discussion concerning the evolution of the calcite phase during the interactive process with the SBF. The formation of a calcite crystalline phase is clearly displayed in both bioglasses from the first hour, as shown in **Fig. 4**. Following the interaction for three days, these peaks have moved towards the positions of peaks corresponding to phosphate phases (indicated by grey lines). This clearly shows that both MBGs exhibit changes in their local structure, evolving towards the reference

structures of bone and the crystalline HCA phase, albeit a slightly shifted peak position (less than 0.1 Å) compared to bulk HCA. This tiny shift could suggest a slight relaxation of the structure of the confined phases within nanopores compared to bulk crystalline HCA. In fact, such relaxation has also been observed in the previous studies of confined molecules in a mesoporous silica matrix [57].

To summarize, the PDF analysis in this work indicates the presence of amorphous calcium phosphate ACP and/or H(C)A phase on both bioglasses from the initial stages of interaction with c-SBF solution. Thus, in order to confirm this hypothesis, a complementary analysis by Raman spectroscopy has been conducted.

Fig. 5 (a)(b) display the Raman spectra of 58S and 70S30C, respectively, after being soaked in conventional SBF. The spectral range considered is between 400 and 1300 cm^{-1}, which includes the main vibrational bands of silica and phosphate phases [65]. According to literature [65], the presence of crystalline carbonate hydroxyapatite (HCA) is indicated by P-O bands at 435, 590, 960, and 1075 cm^{-1} while the amorphous phase ACP is identifiable by broader P-O bands at 630, 950, and 1080 cm^{-1}. Thus, by examining the position and the shape of these peaks, the various phosphate phases can be distinguished. Moreover, the presence of the calcite phase can be identified through the presence of a band at 1087 cm^{-1}, which corresponds to the symmetric stretching mode of carbonate ions. In this study, for the dry binary BG (70S30C), the

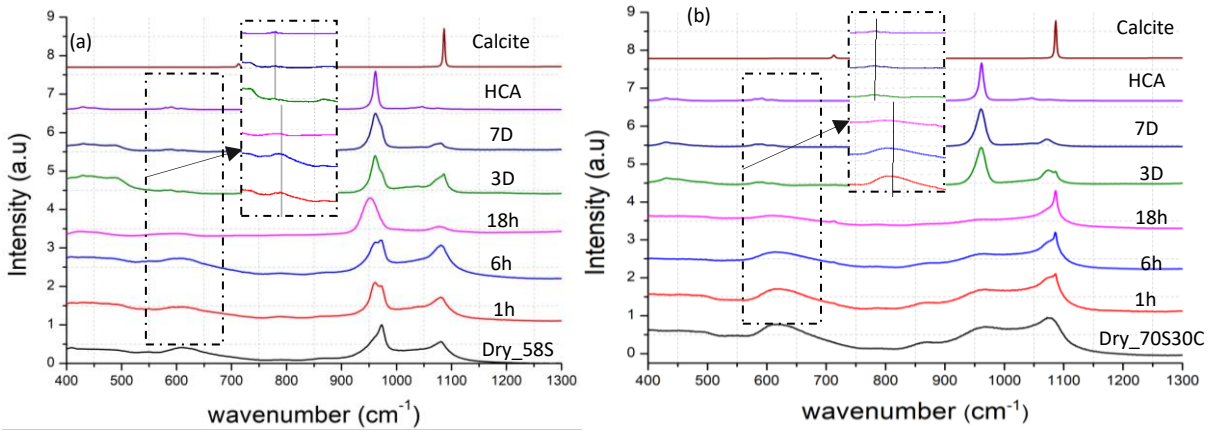

Fig. 5. Raman Spectra of BGs 58S (a) and 70S30C (b) before and after the contact with the c-SBF for different immersion durations and compared to the commercial calcite and HCA.

broad bands that are observed between 520-750, 820-1000, and between 1000-1200 cm^{-1} can be assigned to different molecular vibrations modes. For instance, the first band corresponds to the deformation mode of the Si-O-Si group, the second band indicates the symmetric stretching modes of the Si-O-Si bond with different non-bridging oxygens, and the third to the asymmetric stretching of Si-O-Si fragments [66].

For the spectrum of the dry ternary BG (58S), a broad band is observed, characterized by a sharp maximum at 971 cm^{-1} and a shoulder at 957 cm^{-1}, indicative of the symmetric stretching modes of the Si-O-Si bond and PO_4^{3-} group. Additionally, a peak at 1074 cm^{-1} is associated with the antisymmetric stretching mode of PO_4^{3-}. These

bands indicate thus the presence of a phosphate phase in the dry silicate BG (58S). Upon one-hour contact of 58S BG with c-SBF (see **Fig.5(a)**), the shoulder at 957 cm^{-1} transforms into a clearly visible peak at 955 cm^{-1}, that can be associated to a phosphate phase, more specifically the ACP phase. With increasing immersion time, this peak starts to move towards 960 cm^{-1}, indicating the formation of an apatite phase (H(C)A) on the surface of the ternary 58S BG. This observation is consistent with the PDF results (see **Fig. 4.**), where we were able to detect the presence of the phosphate phase from the early stages, and detect its transformation into a crystalline H(C)A phase. This crystalline phosphate phase reaches its maximum over a period of 7 days. Furthermore, the formation of calcium carbonate (calcite) starts after 1 h of contact with c-SBF and then almost disappears within one week.

In contrast, in the case of binary BG (70S30C) (**Fig. 5(b)**), the intensities of the bands associated to the vibrational modes of Si-O-Si decrease with increasing soaking times. The presence of the calcite phase was also observed in the initial stages of immersion, increasing until 18h followed by a subsequent reduction within one week. After a period of 3 days, the hydroxyapatite phase became visibly noticeable without any clear prior indication.

In order to corroborate further our findings, SEM analysis was performed on both BGs with different interaction times. Initially, the dry MBGs have a smooth texture on their surfaces (**Fig. 3.**). Upon being submerged in SBF, the surfaces begin to gradually roughen and become covered with a layer of phosphate phase and/or calcite (**Fig. 6.**). These phases have been successfully identified from the d-PDF analysis (**Fig. 4.**) after just one hour of immersion, specifically in the case of the binary glass (70S30C).

Furthermore, we performed EDS analysis on the areas indicated by rectangles in **Fig. 6(b)(d)**, confirming the presence of a ratio of calcium and phosphore similar to that found in ACP and H(C)A phases. Further information on EDS analysis is given in the

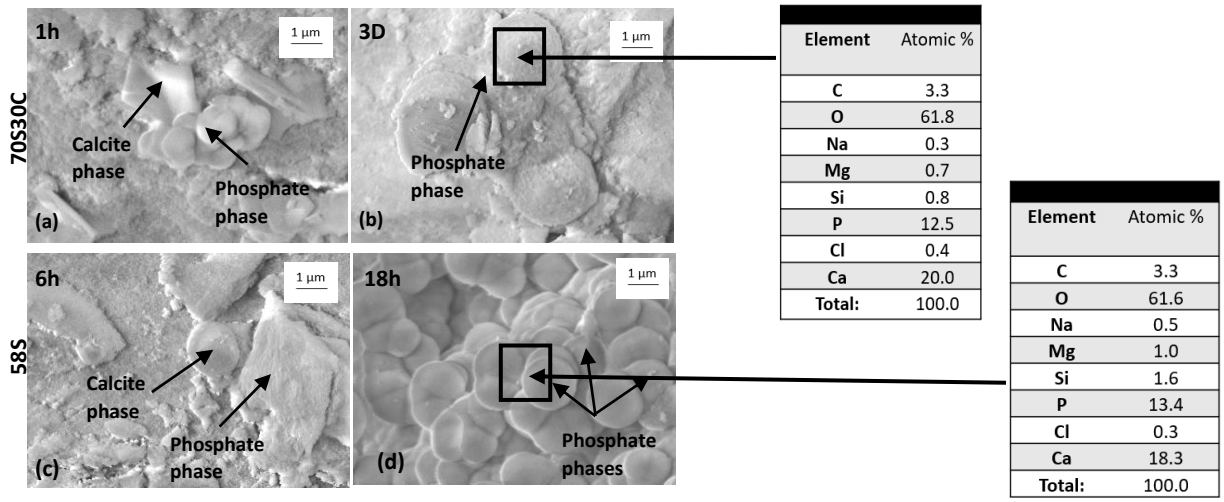

Fig. 6. SEM images of BGs 70S30C (a)(b) and 58S (c)(d) after being soaked in c-SBF with different immersion times. EDS analysis was done on the whole rectangle area of both images (b) and (d). (The elementary analysis error may reach to 5%).

supplementary information.

4. Discussion:

In the d-PDF analysis (**Fig. 4**), we were able to track the formation of the phosphate phases from the first hour of immersion of the binary glass 70S30C (**Fig. 4(b)**), whereas the sole Raman results are not unambiguous due to the contribution of multiple phases (silica, ACP…) in the region 925-975 cm^{-1}. For further detailed analysis on the presence of the ACP phase, we performed a spectral decomposition in the region 800-1100 cm^{-1} (more details are given in the supplementary material). **Fig. 7.** presents the evolution of three phases: ACP, CC, and H(C)A from the decomposition of Raman and PDF data over different immersion times for both prototypical BGs (58S and 70S30C). The evolution of the silicate phase is given in the supplementary material. As can be seen from this figure, there is a good agreement between the deconvolution of PDF and Raman analysis when studying the formation and development of different phases on the surface of bioglasses over various soaking times. Both analyses show the same tendency in the evolution of different species in the binary (70S30C) and ternary (58S) glasses but their quantities slightly differ. This difference can be attributed to the different types of information analyzed by each technique: local information from Raman spectroscopy and global information from PDF analysis. The presence of two phases, namely amorphous calcium phosphate (ACP) and calcite (CC) phases appear immediately after the direct contact of both BGs with synthetic physiological fluid. Over a period of 18h, the ACP phase reaches the highest amount, while the H(C)A phases cannot be unambiguously detected. Subsequently, there is a notable drop in the amounts of ACP, particularly in the case of 70S30C, followed by a significant raise in the H(C)A phases (**Fig. 7(a)**). These findings provide a clear evidence that the ACP phase undergoes a direct transformation into the H(C)A phase, suggesting that ACP serves as main precursor for the nucleation of the apatite mineral phase. Note that the ACP concentration in the ternary BG (58S) exhibits only a slight drop with the still significant raise in H(C)A concentration (**Fig. 7(c)(d)**). This tiny reduction of the ACP phase can be explained by the continuous formation of this amorphous phase even after a period of 3 days, due to the presence of two sources of phosphorous: the SBF solution and the BG itself (58S). Contrary to that, in the binary BG (70S30C), there is only one source of phosphate (from the solution), resulting in a more significant reduction of the ACP amounts within 3 days of immersion. These insights can be considered as evidence to support Hench's theory. According to this mechanism, the ACP phase starts to form prenucleation clusters on the surface of BGs directly after interaction with SBFs. Then, these clusters aggregate to form ACP particles, which eventually grow and transform into H(C)A phase. This has also been demonstrated in previous works [43,67], where the initial formation of ACP layer on the BGs and its subsequent crystallization after 1-3 days were detected by using Small angle X-ray scattering (SAXS) and Fourier

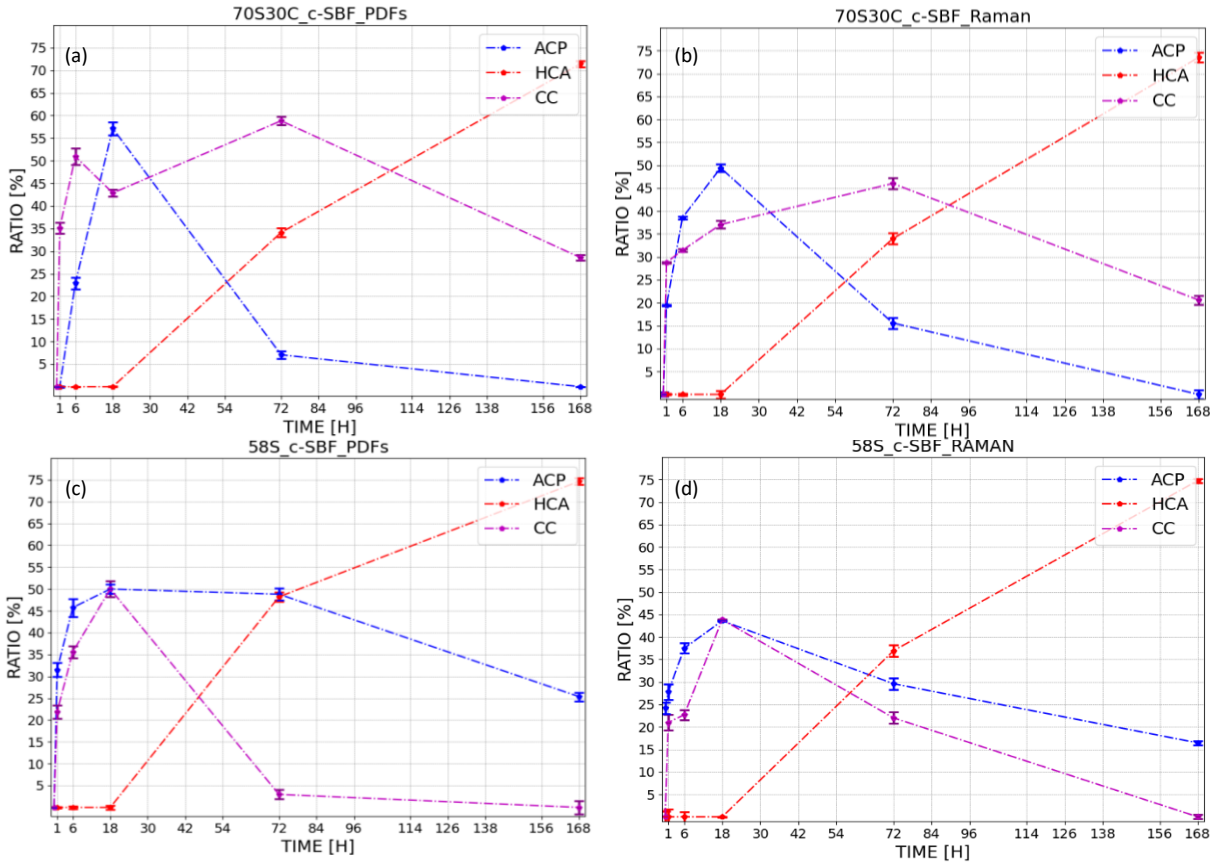

Fig. 7. Single-value decomposition results for the three phases ACP, HCA, and CC, as obtained from PDF analysis for 70S30C (a) and 58S (c) and Raman spectroscopy for 70S30C (b) and 58S (d).

transform infrared reflection spectroscopy. Moreover, in the case of 70S30C, the calcium carbonate (CC) phase increased continuously until it reached saturation within 3 days in contact with c-SBF solution, unlike in the case of ternary 58S BG, where there is a significant reduction of the CC phase after 18h. This difference can be explained by the presence of phosphorous in low amounts in the binary case, favorizing the formation of calcite in the available nucleation sites where they persist even after 7 days. This is a clear evidence of the presence of a competition between ACP and calcium carbonate in occupying the free nucleation sites on the BGs' surfaces. Thus, the presence of a high phosphorous amount is essential in promoting the formation of the crystalline H(C)A phase, which in the course of the reaction contribute in reducing the development of crystalline calcite phases. The drop of the calcite phase in the ternary glass (58S) after 18h followed by an increase of H(C)A with slight decrease of ACP, suggests a transformation of the calcite phase, possibly towards ACP, due to the incorporation of the remaining phosphorous ions from the solution. This phenomenon has also been described in the studies of Sun Yanyan et *al.* [68], where the calcite (CC) transformed into the H(C)A phase through the prolonged soaking times in a phosphate solution like K_2HPO_4.

Furthermore, note that by combining these findings with the EDS analysis, we can attribute the presence of phosphate phases in the earlier stages (1h to 18h) as shown

in **Fig. 6(a)(c)(d)** to the presence of amorphous ACP species and the phosphate phases in **Fig. 6(b)** to crystalline apatite (H(C)A). The presence of silicon (Si) in these areas can be attributed to the silica gel layer that precipitate under the phosphate phases. To conclude, by referring to our previous discussion, we can confirm that the presence of smaller amounts of phosphate phases (**Fig. 6.**) on both BGs in the earlier immersion stages can be attributed to the presence of an amorphous calcium phosphate (ACP) instead of crystalline phases. So, by considering all the results, we can study the evolution of all the phases step by step from the first hour in order to evaluate the behavior of bioglasses *in-vitro* and confirming the Hench transformation path of the crystalline phosphate phases.

5. Conclusion:

In summary, by using the d-PDF analysis coupled with Raman data, we were able to monitor the evolution of the various structural phases forming on the BGs' surfaces over different immersion times. In particular, the amorphous calcium phosphate (ACP) and crystalline calcium carbonate (CC) phases were tracked in the two investigated BGs (58S and 70S30C), revealing a competition between them in the occupation of the nucleation sites followed by a gradual transformation into a mineral-like phase named H(C)A. It is also essential to highlight in this context the possibility of the transformation of CC into ACP before ultimately becoming H(C)A. This coupled analytical approach presents thus a clear scenario on the conversion process of ACP to H(C)A on the surface of the biomaterial. After 18h of immersion in c-SBF, the ACP clusters remain in contact with both BGs (58S and 70S30C) surfaces and subsequently undergo a structural transformation into H(C)A. This indicates that ACP involves a rearrangement of the structure without the need to dissolve into the solution prior to the apatite formation. Moreover, this analysis shows that CC does not limit the apatite formation process, but slows down its kinetics. So, in order to promote apatite growth, one should limit the formation of CC in the initial stage of BGs' immersion. Overall, our study shows that consistent quantitative information on the phases involved in H(C)A formation can be obtained from deconvoluted differential PDF and Raman spectra. The approach employed in this work could therefore be used for effective assessment of the bioactive response of various biomaterials, particularly during the early stages of their interaction with the physiological environment.

CRediT authorship contribution statement:

Amira Ghneim: Writing – original draft, Visualization, Investigation. Lea Abou Samra: Visualization, Investigation. Dominik Schaniel: Writing, Investigation. Samantha Soule: SEM and EDS measurements and analysis. Cédric Carteret: Raman Measurements. El-Eulmi Bendeif: Writing, correcting, d-PDF analysis, Investigation.

Acknowledgements:

We would like to thank Lionel Richaudeau from (L2CM) Laboratory at Lorraine University for providing a crystalline carbonate hydroxyapatite as a sample reference. We acknowledge Swiss Light Source (SLS) and Soleil for providing synchrotron radiation, and we want to thank Dr. Antonio Cervellino for the synchrotron measurements using Material Science (MS) beamline at SLS as well as Dr. Erik Elkaim for his assistance in using Cristal beamline at Soleil (*project number 20220732*). The authors wish to express their deepest thanks to Dr. Bertrand Fournier from the Institut Galien Paris-Sacaly, for his invaluable help with the SVD analysis.

The authors would like to thank the PMD²X X-ray diffraction facility of the CRM² laboratory (*https://crm2.univ-lorraine.fr/plateformes/pmd2x/),* Université de Lorraine, for preliminary X-ray diffraction measurements. Authors also thank the Spectroscopy and Microscopy Service Facility (SMI) of LCPME (Université de Lorraine-CNRS: *https://www.lcpme.ul.cnrs.fr/)* for the SEM-EDS and Raman analyses.

A.G. is indebted to the French Ministry of Higher Education and Research and Université de Lorraine for a doctoral fellowship.

References:

[1] L.L. Hench, R.J. Splinter, W.C. Allen, T.K. Greenlee, Bonding mechanisms at the interface of ceramic prosthetic materials, J. Biomed. Mater. Res. 5 (1971) 117–141. https://doi.org/10.1002/jbm.820050611

[2] L.L. Hench, J. Wilson, Surface-Active Biomaterials, Science 226 (1984) 630–636. https://doi.org/10.1126/science.6093253

[3] M.H. Kaou, M. Furkó, K. Balázsi, C. Balázsi, Advanced bioactive glasses: the newest achievements and breakthroughs in the area, Nanomaterials 13 (2023) 2287. https://doi.org/10.3390/nano13162287

[4] T.M. Koushik, C.M. Miller, E. Antunes, Bone Tissue Engineering Scaffolds: Function of Multi-Material Hierarchically Structured Scaffolds, Adv. Healthc. Mater. 12 (2023) 2202766. https://doi.org/10.1002/adhm.202202766

[5] C. Huang, M. Yu, H. Li, X. Wan, Z. Ding, W. Zeng, Z. Zhou, Research progress of bioactive glass and its application in orthopedics, Adv. Mater. Interfaces 8 (2021) 2100606. https://doi.org/10.1002/admi.202100606

[6] H.E. Skallevold, D. Rokaya, Z. Khurshid, M.S. Zafar, Bioactive glass applications in dentistry, Int. J. Mol. Sci. 20 (2019) 5960. https://doi.org/10.3390/ijms20235960

[7] P.A. Dash, S. Mohanty, S.K. Nayak, A review on bioactive glass, its modifications and applications in healthcare sectors, J. Non-Cryst. Solids 614 (2023) 122404. https://doi.org/10.1016/j.jnoncrysol.2023.122404

[8] J.R. Jones, Review of bioactive glass: from Hench to hybrids, Acta Biomater. 9 (2013) 4457–4486. https://doi.org/10.3390/ijms20235960

[9] Q.Z. Chen, I.D. Thompson, A.R. Boccaccini, 45S5 Bioglass®-derived glass–ceramic scaffolds for bone tissue engineering, Biomaterials 27 (2006) 2414–2425. https://doi.org/10.1016/j.biomaterials.2005.11.025

[10] K. Deshmukh, T. Kovarık, T. Krenek, D. Docheva, T. Stich, J. Pola. Recent advances and future perspectives of sol–gel derived porous bioactive glasses: a review RSC Adv. 10 (2020) 33782. https://doi.org/10.1039/d0ra04287k

[11] G. J. Owens, R. K. Singh, F. Foroutan, M. Alqaysi, C.-M. Han, C. Mahapatra, H.-W. Kim, J. C. Knowles. Sol–gel based materials for biomedical applications. Progress in Materials Science 77 (2016) 1–79. https://doi.org/10.1016/j.pmatsci.2015.12.001

[12] S. Gupta, S. Majumdar, S. Krishnamurthy. Bioactive glass: A multifunctional delivery system. Journal of Controlled Release 335 (2021), 481-497. https://doi.org/10.1016/j.jconrel.2021.05.043

[13] S. Tangri, N. Hasan, J. Kaur, S. Maan, P. Kesharwani, F.J. Ahmad, others, Drug loaded bioglass nanoparticles and their coating for efficient tissue and bone regeneration, J. Non-Cryst. Solids 616 (2023) 122469. https://doi.org/10.1016/j.jnoncrysol.2023.122469

[14] R.A. Martin, S. Yue, J.V. Hanna, P. Lee, R.J. Newport, M.E. Smith, J.R. Jones, Characterizing the hierarchical structures of bioactive sol–gel silicate glass and hybrid scaffolds for bone regeneration, Philos. Trans. R. Soc. Math. Phys. Eng. Sci. 370 (2012) 1422–1443. https://doi.org/10.1098/rsta.2011.0308

[15] L.L. Hench, Chronology of bioactive glass development and clinical applications, (2013). http://dx.doi.org/10.4236/njgc.2013.32011

[16] L.L. Hench, Bioceramics: from concept to clinic, J. Am. Ceram. Soc. 74 (1991) 1487–1510. https://doi.org/10.1111/j.1151-2916.1991.tb07132.x

[17] Y. Ebisawa, T. Kokubo, K. Ohura, T. Yamamuro, Bioactivity of CaO· SiO 2-based glasses: in vitro evaluation, J. Mater. Sci. Mater. Med. 1 (1990) 239–244. http://dx.doi.org/10.4236/njgc.2013.32011

[18] S. Fujibayashi, M. Neo, H.-M. Kim, T. Kokubo, T. Nakamura, A comparative study between in vivo bone ingrowth and in vitro apatite formation on Na2O–CaO–SiO2 glasses, Biomaterials 24 (2003) 1349–1356. https://doi.org/10.1016/S0142-9612(02)00511-2

[19] M. Cerruti, Surface characterization of silicate bioceramics, Philos. Trans. R. Soc. Math. Phys. Eng. Sci. 370 (2012) 1281–1312. https://doi.org/10.1098/rsta.2011.0274

[20] L. Skipper, F. Sowrey, R. Rashid, R. Newport, X-ray diffraction and solid state NMR studies of the, Phys. Chem. Glas. 46 (2005).

[21] C. Turdean-Ionescu, B. Stevensson, J. Grins, I. Izquierdo-Barba, A. Garcia, D. Arcos, M. Vallet-Regi, M. Edén, Composition-dependent in vitro apatite formation at mesoporous bioactive glass-surfaces quantified by solid-state NMR and powder XRD, RSC Adv. 5 (2015) 86061–86071. https://doi.org/10.1039/C5RA13410B

[22] P.N. Gunawidjaja, I. Izquierdo-Barba, R. Mathew, K. Jansson, A. Garcia, J. Grins, D. Arcos, M. Vallet-Regi, M. Edén, Quantifying apatite formation and cation leaching from mesoporous bioactive glasses in vitro: a SEM, solid-state NMR and powder XRD study, J. Mater. Chem. 22 (2012) 7214–7223. https://doi.org/10.1039/C2JM15066B

[23] K.S. Lin, Y.-H. Tseng, Y. Mou, Y.-C. Hsu, C.-M. Yang, J.C. Chan, Mechanistic study of apatite formation on bioactive glass surface using 31P solid-state NMR spectroscopy, Chem. Mater. 17 (2005) 4493–4501. https://doi.org/10.1021/cm050654c

[24] S. Hayakawa, K. Tsuru, C. Ohtsuki, A. Osaka, Mechanism of apatite formation on a sodium silicate glass in a simulated body fluid, J. Am. Ceram. Soc. 82 (1999) 2155–2160. https://doi.org/10.1111/j.1151-2916.1999.tb02056.x

[25] E. Dietrich, H. Oudadesse, M. Le Floch, B. Bureau, T. Gloriant, In vitro Chemical Reactivity of Doped Bioactive Glasses: an Original Approach by Solid-State NMR Spectroscopy, Adv. Eng. Mater. 11 (2009) B98–B105. https://doi.org/10.1002/adem.200800400

[26] P.N. Gunawidjaja, A.Y. Lo, I. Izquierdo-Barba, A. Garcia, D. Arcos, B. Stevensson, J. Grins, M. Vallet-Regi, M. Edén, Biomimetic apatite mineralization mechanisms of mesoporous bioactive glasses as probed by multinuclear 31P, 29Si, 23Na and 13C solid-state NMR, J. Phys. Chem. C 114 (2010) 19345–19356. https://doi.org/10.1021/jp105408c

[27] P.N. Gunawidjaja, R. Mathew, A.Y. Lo, I. Izquierdo-Barba, A. García, D. Arcos, M. Vallet-Regí, M. Edén, Local structures of mesoporous bioactive glasses and their surface alterations in vitro: inferences from solid-state nuclear magnetic resonance, Philos. Trans. R. Soc. Math. Phys. Eng. Sci. 370 (2012) 1376–1399. https://doi.org/10.1098/rsta.2011.0257

[28] R. Mathew, P.N. Gunawidjaja, I. Izquierdo-Barba, K. Jansson, A. García, D. Arcos, M. Vallet-Regí, M. Edén, Solid-state 31P and 1H NMR investigations of amorphous and crystalline calcium phosphates grown biomimetically from a mesoporous bioactive glass, J. Phys. Chem. C 115 (2011) 20572–20582. https://doi.org/10.1021/jp206237n

[29] X. Yan, C. Yu, X. Zhou, J. Tang, D. Zhao, Highly ordered mesoporous bioactive glasses with superior in vitro bone-forming bioactivities, Angew. Chem. Int. Ed. 43 (2004) 5980–5984. https://doi.org/10.1002/anie.200460598

[30] X. Yan, X. Huang, C. Yu, H. Deng, Y. Wang, Z. Zhang, S. Qiao, G. Lu, D. Zhao, The in-vitro bioactivity of mesoporous bioactive glasses, Biomaterials 27 (2006) 3396–3403. https://doi.org/10.1016/j.biomaterials.2006.01.043

[31] A. López-Noriega, D. Arcos, I. Izquierdo-Barba, Y. Sakamoto, O. Terasaki, M. Vallet-Regí, Ordered mesoporous bioactive glasses for bone tissue regeneration, Chem. Mater. 18 (2006) 3137–3144. https://doi.org/10.1021/cm060488o

[32] I. Izquierdo-Barba, D. Arcos, Y. Sakamoto, O. Terasaki, A. López-Noriega, M. Vallet-Regí, High-performance mesoporous bioceramics mimicking bone mineralization, Chem. Mater. 20 (2008) 3191–3198. https://doi.org/10.1021/cm800172x

[33] A. García, M. Cicuéndez, I. Izquierdo-Barba, D. Arcos, M. Vallet-Regí, Essential role of calcium phosphate heterogeneities in 2D-hexagonal and 3D-cubic SiO2- CaO-P2O5 mesoporous bioactive glasses, Chem. Mater. 21 (2009) 5474–5484. https://doi.org/10.1021/cm9022776

[34] H. Takadama, H.-M. Kim, T. Kokubo, T. Nakamura, Mechanism of biomineralization of apatite on a sodium silicate glass: TEM- EDX study in vitro, Chem. Mater. 13 (2001) 1108–1113. https://doi.org/10.1021/cm0008718

[35] C. Berbecaru, G. Stan, S. Pina, D. Tulyaganov, J. Ferreira, The bioactivity mechanism of magnetron sputtered bioglass thin films, Appl. Surf. Sci. 258 (2012) 9840–9848. https://doi.org/10.1016/j.apsusc.2012.06.039

[36] F. Branda, R. Fresa, A. Costantini, A. Buri, Bioactivity of 1.25 CaO· SiO2 glass: an FTIR and X-ray study on powdered samples, Biomaterials 17 (1996) 2247–2251. https://doi.org/10.1016/0142-9612(95)00328-2

[37] A. Salinas, A. Martin, M. Vallet-Regí, Bioactivity of three CaO–P2O5–SiO2 sol-gel glasses, J. Biomed. Mater. Res. Off. J. Soc. Biomater. Jpn. Soc. Biomater. Aust. Soc. Biomater. Korean Soc. Biomater. 61 (2002) 524–532. https://doi.org/10.1002/jbm.10229

[38] M. Cerruti, C.L. Bianchi, F. Bonino, A. Damin, A. Perardi, C. Morterra, Surface modifications of bioglass immersed in TRIS-buffered solution. A multitechnical spectroscopic study, J. Phys. Chem. B 109 (2005) 14496–14505. https://doi.org/10.1021/jp050705t

[39] C. Liu, R. Zhang, X. Zhao, J. Jia, Y. Min, Quantification of phosphorus structures in CaO–SiO2– P2O5 glasses via Raman spectroscopy, J. Non-Cryst. Solids 557 (2021) 120579. https://doi.org/10.1016/j.jnoncrysol.2020.120579

[40] J. Lao, J.-M. Nedelec, E. Jallot, New Insight into the Physicochemistry at the Interface between Sol- Gel-Derived Bioactive Glasses and Biological Medium: A PIXE-RBS Study, J. Phys. Chem. C 112 (2008) 9418–9427. https://doi.org/10.1021/jp800583m

[41] J. Soulié, J. Lao, E. Jallot, J.-M. Nedelec, Influence of mesostructuration on the reactivity of bioactive glasses in biological medium: a PIXE-RBS study, J. Mater. Chem. 22 (2012) 20680–20688. https://doi.org/10.1039/C2JM30880K

[42] R. Li, A. Clark, L. Hench, An investigation of bioactive glass powders by sol-gel processing, J. Appl. Biomater. 2 (1991) 231–239. https://doi.org/10.1002/jab.770020403

[43] C.Y. Kim, A.E. Clark, L.L. Hench, Early stages of calcium-phosphate layer formation in bioglasses, J. Non-Cryst. Solids 113 (1989) 195–202. https://doi.org/10.1016/0022-3093(89)90011-2

[44] Ö. Andersson, I. Kangasniemi, Calcium phosphate formation at the surface of bioactive glass in vitro, J. Biomed. Mater. Res. 25 (1991) 1019–1030. https://doi.org/10.1002/jbm.820250808

[45] M. Brink, T. Turunen, R.-P. Happonen, A. Yli-Urpo, Compositional dependence of bioactivity of glasses in the system Na2O-K2O-MgO-CaO-B2O3-P2O5-SiO2, J. Biomed. Mater. Res. Off. J. Soc. Biomater. Jpn. Soc. Biomater. 37 (1997) 114–121. https://doi.org/10.1002/(SICI)1097-4636(199710)37:1%3C114::AID-JBM14%3E3.0.CO;2-G

[46] L. Varila, S. Fagerlund, T. Lehtonen, J. Tuominen, L. Hupa, Surface reactions of bioactive glasses in buffered solutions, J. Eur. Ceram. Soc. 32 (2012) 2757–2763. https://doi.org/10.1016/j.jeurceramsoc.2012.01.025

[47] V. Banchet, E. Jallot, J. Michel, L. Wortham, D. Laurent-Maquin, G. Balossier, X-ray microanalysis in STEM of short-term physicochemical reactions at bioactive glass particle/biological fluid interface. Determination of O/Si atomic ratios, Surf. Interface Anal. Int. J. Devoted Dev. Appl. Tech. Anal. Surf. Interfaces Thin Films 36 (2004) 658–665. https://doi.org/10.1002/sia.1916

[48] M. Cerruti, A. Perardi, G. Cerrato, C. Morterra, Formation of a nanostructured layer on bioglass particles of different sizes immersed in tris-buffered solution. N2 adsorption and HR-TEM/EDS analysis, Langmuir 21 (2005) 9327–9333. https://doi.org/10.1021/la051221r

[49] H. Aguiar, E. Solla, J. Serra, P. González, B. León, F. Malz, C. Jäger, Raman and NMR study of bioactive Na2O–MgO–CaO–P2O5–SiO2 glasses, J. Non-Cryst. Solids 354 (2008) 5004–5008. https://doi.org/10.1016/j.jnoncrysol.2008.07.033

[50] E. Fukushina, T. Sakamoto, H. Takebe, Microstructural investigation of hydroxyapatite formation in bioactive borosilicate glass, J. Ceram. Soc. Jpn. 131 (2023) 843–849. https://doi.org/10.2109/jcersj2.23113

[51] M. Edén, Structure and formation of amorphous calcium phosphate and its role as surface layer of nanocrystalline apatite: Implications for bone mineralization, Materialia 17 (2021) 101107. https://doi.org/101107. 10.1016/j.mtla.2021.101107

[52] V. Fitzgerald, K.O. Drake, J.R. Jones, M.E. Smith, V. Honkimäki, T. Buslaps, M. Kretzschmer, R.J. Newport, In situ high-energy X-ray diffraction study of a bioactive calcium silicate foam immersed in simulated body fluid, J. Synchrotron Radiat. 14 (2007) 492–499. https://doi.org/10.1107/S0909049507042173

[53] M. Mozafari, S. Banijamali, F. Baino, S. Kargozar, R.G. Hill, Calcium carbonate: Adored and ignored in bioactivity assessment, Acta Biomater. 91 (2019) 35–47. https://doi.org/10.1016/j.actbio.2019.04.039

[54] T.H. Dang, T.H. Bui, E.V. Guseva, A.T. Ta, A.T. Nguyen, T.T.H. Hoang, X.V. Bui, Characterization of bioactive glass synthesized by sol-gel process in hot water, Crystals 10 (2020) 529. https://doi.org/10.3390/cryst10060529

[55] A. Oyane, H.-M. Kim, T. Furuya, T. Kokubo, T. Miyazaki, T. Nakamura, Preparation and assessment of revised simulated body fluids, J. Biomed. Mater. Res. Part Off. J. Soc. Biomater. Jpn. Soc. Biomater. Aust. Soc. Biomater. Korean Soc. Biomater. 65 (2003) 188–195. https://doi.org/10.1002/jbm.a.10482

[56] D. Lukito, J. Xue, J. Wang, In vitro bioactivity assessment of 70 (wt.)% SiO2–30 (wt.)% CaO bioactive glasses in simulated body fluid, Mater. Lett. 59 (2005) 3267–3271. https://doi.org/10.1016/j.matlet.2005.05.055

[57] K.-Y. Hsieh, E.-E. Bendeif, A. Gansmuller, S. Pillet, T. Woike, D. Schaniel, Structure and dynamics of guest molecules confined in a mesoporous silica matrix: Complementary NMR and PDF characterisation, RSC Adv. 3 (2013) 26132–26141. https://doi.org/10.1039/C3RA45347B

[58] H. Khoder, D. Schaniel, S. Pillet, E.-E. Bendeif, X-ray scattering study of water confined in bioactive glasses: experimental and simulated pair distribution function, Acta Crystallogr. Sect. Found. Adv. 76 (2020) 589–599. https://doi.org/10.1107/S2053273320007834/vk5044sup1.pdf

[59] P. Juhás, T. Davis, C.L. Farrow, S.J. Billinge, PDFgetX3: a rapid and highly automatable program for processing powder diffraction data into total scattering pair

distribution functions, J. Appl. Crystallogr. 46 (2013) 560–566. https://doi.org/10.1107/S0021889813005190

[60] E. Henry, J. Hofrichter, [8] Singular value decomposition: Application to analysis of experimental data, in: Methods Enzymol., Elsevier, 1992: pp. 129–192. https://doi.org/10.1016/0076-6879(92)10010-B

[61] I. Hammami, S.R. Gavinho, A.S. Pádua, M. do C. Lança, J.P. Borges, J.C. Silva, I. Sá-Nogueira, S.K. Jakka, M.P.F. Graça, Extensive Investigation on the Effect of Niobium Insertion on the Physical and Biological Properties of 45S5 Bioactive Glass for Dental Implant, Int. J. Mol. Sci. 24 (2023) 5244. https://doi.org/10.3390/ijms24065244

[62] M. Thommes, K. Kaneko, A.V. Neimark, J.P. Olivier, F. Rodriguez-Reinoso, J. Rouquerol, K.S. Sing, Physisorption of gases, with special reference to the evaluation of surface area and pore size distribution (IUPAC Technical Report), Pure Appl. Chem. 87 (2015) 1051–1069. https://doi.org/10.1515/pac-2014-1117

[63] L.J. Skipper, F.E. Sowrey, D.M. Pickup, K.O. Drake, M.E. Smith, P. Saravanapavan, L.L. Hench, R.J. Newport, The structure of a bioactive calcia–silica sol–gel glass, J. Mater. Chem. 15 (2005) 2369–2374. https://doi.org/10.1039/B501496D

[64] S.M. Clark, B. Colas, D.E. Jacob, J.C. Neuefeind, H.-W. Wang, K.L. Page, A.K. Soper, P.I. Schodder, P. Duchstein, B.A. Zubiri, others, The nano-and meso-scale structure of amorphous calcium carbonate, Sci. Rep. 12 (2022) 6870. https://doi.org/10.1038/s41598-022-10627-9

[65] G. Sauer, W. Zunic, J. Durig, R. Wuthier, Fourier transform Raman spectroscopy of synthetic and biological calcium phosphates, Calcif. Tissue Int. 54 (1994) 414–420. https://doi.org/10.1007/BF00305529

[66] D. Bellucci, G. Bolelli, V. Cannillo, A. Cattini, A. Sola, In situ Raman spectroscopy investigation of bioactive glass reactivity: Simulated body fluid solution vs TRIS-buffered solution, Mater. Charact. 62 (2011) 1021–1028. https://doi.org/10.1016/j.matchar.2011.07.008

[67] R.A. Martin, H. Twyman, D. Qiu, J.C. Knowles, R.J. Newport, A study of the formation of amorphous calcium phosphate and hydroxyapatite on melt quenched Bioglass® using surface sensitive shallow angle X-ray diffraction, J. Mater. Sci. Mater. Med. 20 (2009) 883–888. https://doi.org/10.1007/s10856-008-3661-5

[68] S. Yanyan, W. Guangxin, L. Wuhui, W. Yaming, S. Hayakawa, A. Osaka, Conversion of sub-μm calcium carbonate (calcite) particles to hollow hydroxyapatite agglomerates in K2HPO4 solutions, Nanotechnol. Rev. 9 (2020) 945–960. https://doi.org/10.1515/ntrev-2020-0070